Journal of Polymers and the Environment (2026) 34:112
https://doi.org/10.1007/s10924-026-03836-0

ORIGINAL PAPER

Fabrication and Characterization of Sodium Carboxymethylcellulose Nanoparticles from *Eichhornia crassipes* Stem

Samy A. Elsayed[1] · **M. A. Elhady**[2] · **A. K. Tammam**[3]

Received: 5 December 2025 / Accepted: 3 April 2026 / Published online: 29 April 2026
© The Author(s) 2026

Abstract

This study presents an innovative method for extracting sodium carboxymethyl cellulose nanoparticles (Na-CMC NPs) from the lignocellulosic biomass of water hyacinth (*Eichhornia crassipes*). The process consists of two major stages: cellulose extraction and Na-CMC synthesis, followed by nanoparticle precipitation. Structural analysis confirmed the success of the extraction process, with X-ray diffraction (XRD) revealing a semi-crystalline structure with a high degree of crystallinity (81 ± 1) % and nanoparticle sizes (11–40) nm. Fourier-transform infrared (FTIR) and NMR spectroscopy verified the substitution pattern and molecular structure. Thermal gravimetric analysis (TGA) identified four distinct decomposition stages, indicating good thermal stability. For the first time, the dielectric properties of Na CMC NPs derived from water hyacinth were thoroughly investigated revealing a correlated barrier hopping (CBH) conduction mechanism with a relaxation activation energy of 0.12 ± 0.05 eV. Morphological characterization by scanning electron microscopy (SEM) and transmission electron microscopy (TEM) confirmed the formation of nanoparticles with diameters ranging from (50–200) nm. The yield of Na-CMC NPs was 62 ± 3%, with a degree of substitution of 0.68. These findings highlight the potential of converting an invasive species into a functional biopolymer nanomaterial with tunable properties for potential applications in electronics, packaging, or as a sustainable polymer matrix. The work establishes a foundation for further exploration of Na-CMC NPs in specific industrial applications.

Keywords Water hyacinth · Sodium carboxymethylcellulose · Dielectric properties · Thermal analysis · Correlated barrier hopping · Biomass valorization

Introduction

The increasing demand for sustainable polymeric materials has intensified interest in cellulose-based derivatives derived from renewable biomass. *Eichhornia crassipes* (water hyacinth) is a highly invasive aquatic plant, causing significant ecological and socioeconomic challenges in tropical regions, including Egypt, by depleting water resources, hindering navigation, and reducing biodiversity [1–3]. However, its rapid proliferation and high biomass yield present a unique opportunity for valorization as a renewable feedstock. Notably, water hyacinth stems contain a high cellulose content (approximately 72%), making them a promising low-cost source for producing cellulose derivatives [4–6]. Carboxymethyl cellulose (CMC), an anionic water-soluble polysaccharide ether, is widely used in food, pharmaceuticals, textiles, and paper industries due to its biodegradability, non-toxicity, and functionality as a thickener, stabilizer, and film-forming agent [7, 8]. Recent

✉ A. K. Tammam
akamel@sci.cu.edu.eg

Samy A. Elsayed
samy.abdelhameed@science.bsu.edu.eg

M. A. Elhady
mohamedelhady2000@yahoo.com

[1] Physics Department, Faculty of Science, Beni Suef University, Beni Suef, Egypt

[2] Polymer Chemistry Department, National Center for Radiation Research and Technology, Egyptian Atomic Energy Authority, Cairo, Egypt

[3] Physics Department, Faculty of Science, Cairo University, Giza, Egypt

advancements focus on Nano cellulose and its derivatives for high-value applications, including antimicrobial packaging, wound dressings, and advanced composites [9–11]. Synthesizing CMC in nanoparticle form can enhance properties like surface area, reactivity, and dispersion, opening avenues in nanomedicine, controlled release, and nanocomposites [6, 12–15].

While the extraction of cellulose and synthesis of CMC from various biomass sources are well documented, the specific conversion of *E. crassipes* cellulose into well-characterized Na-CMC nanoparticles, coupled with an in-depth analysis of their dielectric behavior, remains underexplored [13]. Most studies focus on chemical yield and basic characterization, leaving a gap in understanding the fundamental electrical and polarization properties of this biopolymer, which are crucial for applications in sensors, energy storage, and electronic materials [12, 14].

Furthermore, although *E. crassipes* is known for phytoremediation and may contain absorbed metal ions, their impact on the structural and functional properties of derived CMC, especially at the nanoscale, is not well understood. This study aims to address these gaps. The primary objectives are: (1) to develop and optimize a method for synthesizing Na-CMC NPs from *E. crassipes*; (2) to comprehensively characterize the structural, thermal, morphological, and compositional properties of the product; and (3) to investigate, for the first time, the dielectric and electrical conductivity mechanisms of this material. By transforming an environmental nuisance into a value-added nanomaterial and elucidating its inherent properties, this work contributes to sustainable biomass utilization and advances the fundamental knowledge of biopolymer physics.

Materials

Eichhornia crassipes Fresh specimens of (water hyacinth) were gathered from the banks of the Nile River and adjacent irrigation canals of Egypt. This plant serves as a sustainable and abundant raw material for the extraction of carboxymethyl cellulose. Sodium hydroxide (NaOH), glacial acetic acid (CH_3COOH), and toluene were obtained from El-Gomhoreya Co., Egypt, and were used for alkaline treatment and purification. Ethanol, sodium chlorite ($NaClO_2$), isopropanol and acetone were obtained from "Qualikems Fine Chemicals Pvt. Ltd." New Delhi, India. Monochloroacetic acid ($ClCH_2COOH$) was sourced from Piochem Co., Egypt, and is essential for the carboxymethylation process to achieve the intended chemical modification of cellulose.

Synthesis of Sodium Carboxymethyl Cellulose (Na-CMC)

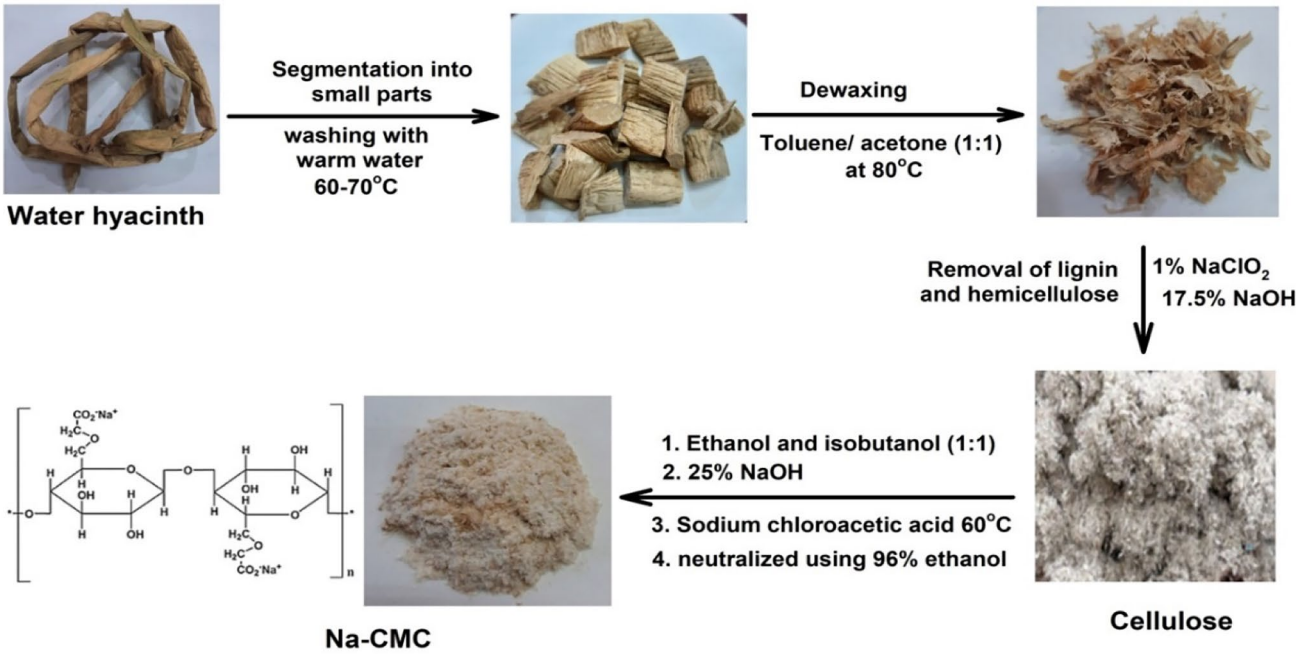
Stage 1: Cellulose Extraction from Water Hyacinth. Fresh stems were chopped (1–2 mm), washed with warm water, and dried at 65 °C for 3 h. Dewaxing was carried out using a 1:1 toluene/acetone mixture at 80 °C for 3 h. The solid residue was then treated with a 1 wt% $NaClO_2$ solution (pH 3–4, adjusted with acetic acid) at 80 °C for 2 h to remove lignin. Subsequently, hemicellulose was removed by treatment with 17.5 wt% NaOH at 80 °C for 2 h. The resulting cellulose was washed with distilled water until neutral pH and dried [16]. The cellulose extraction yield was calculated as 58 ± 2% relative to the dry mass of the initial stems.

Stage 2: Carboxymethylation and Nanoparticle Formation. The extracted cellulose (5.0 g) was suspended in 50 mL of a 50:50 ethanol/isopropanol mixture. Alkalization was performed by adding 6.25 g of NaOH (in 12.5 mL of H_2O, corresponding to a 25% w/v solution) dropwise under vigorous stirring at room temperature for 1 h. Carboxymethylation was initiated by adding 7.5 g of monochloroacetic acid dissolved in 15 mL isopropanol. The reaction mixture was heated to 65 °C and maintained for 3 h with continuous stirring. The crude Na-CMC was neutralized with glacial acetic acid, filtered, and washed sequentially with 80% and 96% ethanol to remove by-products. The purified Na-CMC was dried at 60 °C. The Na-CMC synthesis yield was 62 ± 3% relative to the mass of extracted cellulose [17].

Nanoparticle Preparation: The bulk Na-CMC was converted to nanoparticles via a nanoprecipitation method. A 0.5% (w/v) aqueous solution of Na-CMC was prepared under stirring. This solution was then added dropwise (1 mL/min) into a ten-fold excess of ethanol under high-speed homogenization (10,000 rpm for 15 min). The resulting nanoparticle suspension was collected by centrifugation (12,000 rpm, 20 min), washed with ethanol, and lyophilized to obtain Na-CMC NPs. samples are then purified and neutralized using 96% ethanol as shown in Scheme 1. Finally, the Na-CMC nanoparticles hydrogel was crosslinked using gamma rays of at a dose rate of 0.718 kGy/h.

Experimental Techniques

The infrared (IR) absorption spectrum spanning the range of 4000–400 cm^{-1} was recorded using an FTIR 4100 spectrometer (Jasco-Japan) at the Microanalysis Center of the University of Cairo. Nuclear Magnetic Resonance (NMR) spectra were obtained utilizing a Varian Mercury VX-300 NMR Spectrometer, with ^1H spectra conducted at 300 MHz in deuterated chloroform ($CDCI_3$) or deuterated dimethylsulphoxide (DMSO-d_6). Chemical shifts are expressed in δ (ppm) and referenced to the solvents employed. Surface



Scheme 1 Schematic diagram of Na-CMC NPs synthesis from water hyacinth

morphology was examined using a high-resolution scanning electron microscope (SEM) (HR-SEM; ZEISS EVO 15, UK). Prior to imaging, the samples were coated with a thin layer of gold using spray deposition. The elemental composition was analyzed using energy-dispersive X-ray spectroscopy (EDAX) with an EDAX detector integrated with the ZEISS EVO 15 scanning electron microscope (UK). Particle size and size distribution were analyzed by transmission electron microscopy (TEM; JEOL JSM-100CX, Japan) operated at an accelerating voltage of 80 kV. X-ray diffraction: XRD patterns was recorded using a Shimadzu diffractometer (Tokyo, Japan), XRD-6000 X-ray diffraction spectrometer with a copper target (λ = 1.542 Å), at an operating voltage of 40 kV and an electric current of 30 mA. The XRD patterns were systematically obtained within 2θ = (10–80)° angular range, with a scanning rate of four steps per minute. Differential Scanning Calorimetry (DSC) measurements were conducted using a Q20P system, capable of providing precise heat flow measurements for materials over a temperature range of 232 ± 2 K to 412 ± 2 K, with a heating rate of 5 °C/min. Thermogravimetric analysis (TGA) Thermogravimetric analysis (TGA) was performed with a Shimadzu TGA-50 framework (Kyoto, Japan) in the temperature range 0 °C to 1000 °C at a heating rate of 10 °C/min, accompanied by a steady flow of dry nitrogen gas at a rate of 50 ml/min. Calibration of the system was achieved utilizing the phase transition at the melting point of indium, precisely at 429.9 K. A powdered sample weighing 2.45 mg was utilized. Impedance spectroscopic measurements were executed using a computer-controlled lock-in amplifier (model SR 830) within a nitrogen atmosphere. The samples were prepared in the form of compressed pellets, measuring 10 mm in diameter and 1.0 mm in thickness, and were coated with silver paste to ensure optimal electrical contact. Temperature monitoring was accomplished using a copper-constantan thermocouple, with specific control maintained between 298 and 413 K, exhibiting a stability of ± 0.5 K. The measurements were conducted across a frequency range of 12 Hz to 65 kHz, under an applied potential of 1 V.

Gamma irradiation was performed using a cobalt-60 source at the Canadian Gamma Cell located at the National Center for Radiation Research and Technology (NCRRT), Cairo, Egypt. Irradiation was carried out at 10 kGy with a dose rate of 0.7 kGy/h. Water absorption measurement: The dried sample was weighed and then soaked in water for 24 h to reach absorption equilibrium. The swollen hydrogel was periodically taken out of the water and any surface moisture was blotted off using filter paper. The degree of swelling, defined by grams of water per gram of dry polymer (g/g), was determined by the following equation [18]:

$$\text{Water absorbency}\left(\frac{\text{g wet}}{\text{g dry}}\right)=\left(\frac{W_t-W_0}{W_0}\right)$$

where W_t is the weight of the swollen gel at time t (g), and W_o is the initial dry weight of the gel (g).

Results and Discussion

Structure Properties

X-ray Diffraction

X-ray diffraction (XRD) analysis was employed to investigate the crystalline structure and crystallinity of the raw water hyacinth and the synthesized Na-CMC. The diffraction pattern of water hyacinth (Fig. 1a) exhibits characteristic peaks at 2θ ≈ 15.7° and 21.2°, which are attributed to the typical reflections of cellulose I, confirming the semicrystalline nature of native cellulose. These peaks are consistent with well-established literature on lignocellulosic biomass. In addition to these reflections, the raw sample shows broad diffraction features, indicating the presence of amorphous components such as lignin and hemicellulose [19]. The removal of these amorphous constituents during chemical treatment leads to structural modification of cellulose. The XRD pattern of the synthesized Na-CMC nanoparticles (Na-CMC NPs) displays a significant change in structure, characterized by a broad and diffuse peak in the range of

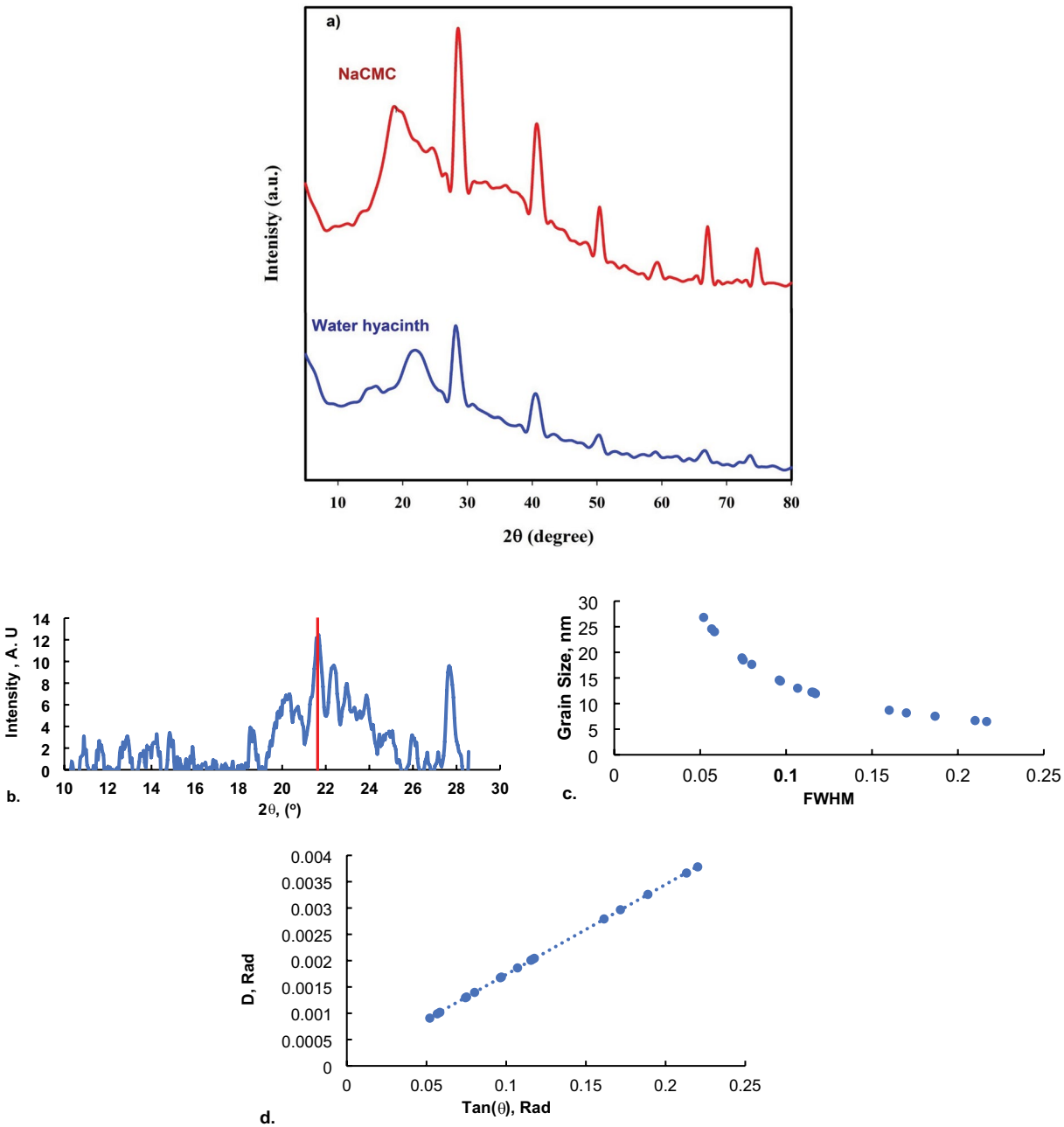


Fig. 1 **a** X-ray diffraction of the extracted Na-CMC NPs in the range (5 < 2θ(°) < 80). **b** X-ray diffraction of the extracted Na-CMC NPs on enlarged scale (10 < 2θ(°) < 30). **c** Shows the dependence of grain Size on FWHM. **d** Shows the dependence of grain Size on tan (θ)

2θ ≈ (18–23)°. This broadening indicates a reduction in crystallinity and an increase in the amorphous character of the material [20]. This behavior is attributed to the carboxymethylation process, in which hydroxyl groups of cellulose are substituted with carboxymethyl groups (–CH_2COONa). This substitution disrupts the intermolecular hydrogen bonding network within cellulose chains, resulting in decreased structural order. Similar observations have been widely reported for chemically modified cellulose derivatives. Minor diffraction peaks observed at higher angles (2θ > 30°) may be attributed to residual inorganic species. This is consistent with the well-documented phytoremediation ability of water hyacinth (*Eichhornia crassipes*), which can accumulate trace metal ions from contaminated environments. However, these peaks are of low intensity and do not affect the primary structural interpretation. Overall, the XRD results confirm the transformation of native cellulose into Na-CMC NPs, accompanied by a decrease in crystallinity and the formation of a predominantly amorphous structure. The dominant diffraction features clearly indicate that Na-CMC NPs is the principal phase in the synthesized material. The elimination of lignin and hemicellulose enhances the crystallinity of Na-CMC NPs, resulting in sharper characteristic peaks as demonstrated in the X-ray diffraction analysis.

Degree of Crystallinity

Figure 1b shows the X-ray diffraction pattern of (Na-CMC) within the angular range of (10° < 2θ < 30°). Figure 1b reveals that at low angles cellulose exhibits an amorphous structure interspersed with a number of crystallites, a phenomenon also observed in previous findings of Tarabiah et al. [21]. The physical properties of cellulose such as tensile strength, elastic modulus, moisture regain, and chemical reactivity are significantly influenced by the degree of crystallinity [22–24]. In the present work Segal method [25] has been employed to determine the degree of crystallinity X_{CR}

$$X_{CR} = \frac{I_{200} - I_{AM}}{I_{200}} \quad (1)$$

where I_{200} is the peak height of the 200 plane at (2θ ~ 21.68°) which is 12.44, I_{AM} is the minimum between the (200) peak at (2θ ~ 21.68°) and the 110 peak at (2θ = 18°) (in amorphous range) which is 2.38. The calculated value of X_{CR} from Fig. 1b and Eq. (1) is 81 ± 1%. This value is lower than that of native cellulose and reflects partial destruction of crystalline domains caused by carboxymethylation. The reduction in crystallinity is consistent with the increased amorphous character and enhanced water solubility of Na-CMC. Segal et al. found X_{CR} for Cotton fibers ranging from 79 to 76% depending on untreated and treated condition [26].

Grain Size

Using Scherrer formula

$$D = \frac{k\lambda}{m\cos(\theta)} \quad (2)$$

where D represents the grain size, *k* is the Scherrer constant, which typically ranges from 0.62 to 2.08; for the purposes of this study, we have adopted a value of k = 0.9. Additionally, λ is the X-ray wavelength, and m denotes the full width at half maximum (FWHM). As illustrated in Fig. 1c. (FWHM) for all observed peaks is given with the data of X from the XRD diffractometer. The grain size exhibits an inverse relationship with FWHM, exhibiting a significant reduction in grain size from 26.8 nm to 6.5 nm as FWHM decreases. The broadening of X-ray diffraction peaks indicates the presence of lattice strain resulting from lattice defects [27–32]. Figure 1d shows the dependence of full width at half maximum (FWHM) D (in radians) on tan (θ). According to the following equation:

$$D = 2\varepsilon\tan(\theta) \quad (3)$$

where ε is the lattice micro strain. From the slope obtained through the line fitting of the data presented in Fig. 1d, it is determined to be 8.55×10^{-3}. The negative value of micro strain indicates the presence of compressive strain, while a positive value corresponds to tensile strain [30]. These results support the conclusion that carboxymethylation induces structural disorder and reduces crystalline domain size in Na-CMC.

SEM, TEM and EDAX Results

Figure 2a and b shows scanning electron microscopy (SEM) images of Na-CMC NPs and Na-CMC hydrogels after irradiation with a dose of 10 kGy. As observed, the presence of pores on the surface of Na-CMC hydrogels is a key factor contributing to their water absorption capacity. Cavities formed between the interconnected Na-CMC networks facilitate water absorption, while these pores are absent in Na-CMC NPs. In contrast, the SEM image of Na-CMC NPs shows a rough surface with no evidence of a porous structure. Although accurately estimating the particle size from the SEM image poses challenges due to considerable agglomeration, the micrograph generally suggests the presence of small, heterogeneous particles that exhibit a tendency to aggregate. Finally, due to their large pores and

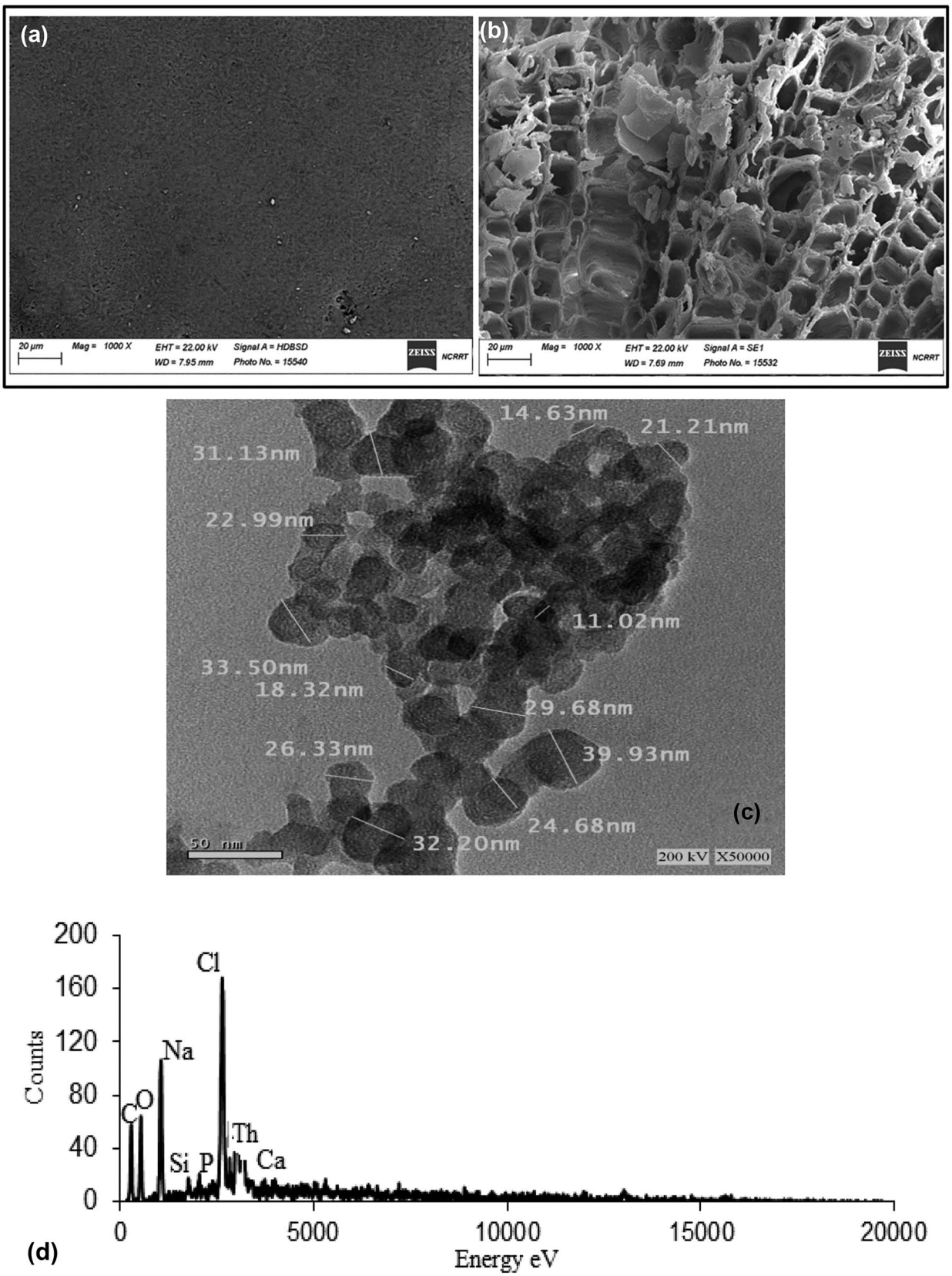


Fig. 2 **a** SEM of the pressed Na-CMC NPs sample. **b** SEM of the pressed Na-CMC hydrogel at 10 kGy. **c** Shows TEM image of Na-CMC NPs. **d** Energy dispersive X-ray analysis of the prepared Na-CMC NPs

Table 1 The EDAX observed elements in the extracted Na-CMC NPs from water Hyacinth (E-Crassipes)

Element	Atomic %	Atomic % Error	Weight %	Weight % Error
C	31.3	0.6	19.6	0.3
O	33.1	1.0	27.79	0.6
Na	27.6	0.3	33.1	0.3
Si	0.9	0.1	1.3	0.1
P	0.6	0.1	1.6	0.1
Cl	5.1	0.3	11.1	0.3
Ca	0.6	0.1	2.3	0.1
Th	0.7	0.3	3.21	0.9

open structure, porous hydrogels exhibit relatively rapid swelling kinetics, with hydrogel samples reaching an equilibrium swelling state within a few minutes to a few hours [33, 34].

In addition to Fig. 2c presents a transmission electron micrograph (TEM) of Na-CMC NPs. The particles exhibit quasi-spherical to irregular morphologies, with average sizes ranging from 11 to 40 nm. (TEM) provides direct, real space imaging of nanoparticle size, shape, and morphology, while (XRD) provides information about the crystalline structure and average crystallite size based on diffraction patterns. Both techniques complement each other, and the TEM observations often reinforce the interpretations drawn from XRD, within acceptable experimental error.

Figure 2d presents the energy-dispersive X-ray (EDX) spectrum of the prepared Na-CMC nanoparticles derived from Eichhornia crassipes. The spectrum confirms the presence of the primary elements expected for sodium carboxymethylcellulose, namely carbon (C), oxygen (O), and sodium (Na), which correspond to the polysaccharide backbone and carboxymethyl functional groups. Table 1 summarizes the detected elemental composition. A minor signal corresponding to chlorine (Cl) is also observed, which can be attributed to residual salts from the synthesis process. In addition to these elements, very weak signals are detected in the higher energy region. Due to their low intensity, these signals are considered trace-level contributions and cannot be conclusively assigned to specific elements or distinct phases. It is important to note that EDX analysis provides semi-quantitative elemental information and has limited sensitivity for the accurate identification and quantification of trace elements or their chemical states. Furthermore, the XRD results do not reveal distinct crystalline phases corresponding to such species, supporting the conclusion that Na-CMC is the dominant material. The observed trace signals, if present, may originate from environmental exposure of the raw biomass or minor residual impurities. However, their negligible intensity indicates that they do not significantly affect the structural integrity or functional performance of the synthesized Na-CMC.

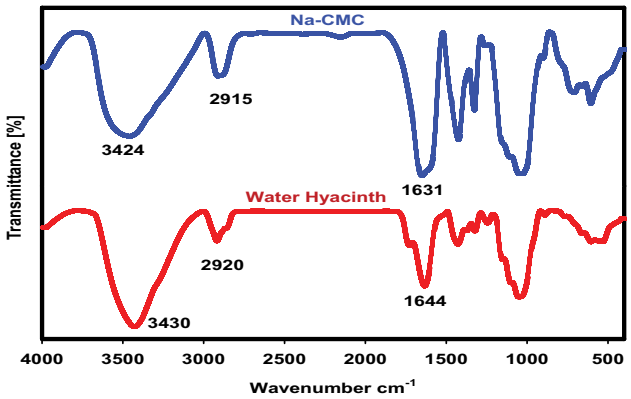


Fig. 3 FTIR transmittance spectrum of the extracted Na-CMC NPs and water hyacinth

The EDX spectrum of the prepared Na-CMC extracted from *Eichhornia crassipes* confirms the presence of thorium together with the main matrix elements (C, O, Na and Cl), indicating that Th is intrinsically associated with the biomass-derived polymer. As summarized in Table 1, thorium accounts for about 3.21 wt%, demonstrating a relatively high enrichment compared with other trace metals. This result is consistent with the well-documented ability of water hyacinth to accumulate thorium from contaminated environments. Previous adsorption studies reported thorium uptakes of about 19–20 mg g^{-1} for leaves and up to 70 mg g^{-1} for roots, confirming the strong affinity of this plant toward Th species. Therefore, the detected Th signal after Na-CMC preparation reflects the retention of naturally adsorbed thorium from the original plant material rather than experimental contamination, validating the EDX interpretation.

IR Spectroscopy

Analysis of Na-CMC NPs and Water Hyacinth by FTIR

Infrared spectroscopy, specifically Fourier Transform Infrared (FTIR) spectroscopy, is an analytical technique used to identify functional groups in organic, polymeric, or coating materials. In this study, FTIR spectroscopy was employed to confirm the functional groups present in Na-CMC NPs and water hyacinth. Water hyacinth cellulose and Na-CMC NPs samples were analyzed using FTIR, and their spectra are presented in Fig. 3. The FTIR spectrum of water hyacinth cellulose shows characteristic absorption bands corresponding to the cellulose backbone. The broad band around 3430 cm^{-1} correspond to (O–H) stretching vibrations, while the band at approximately 2920 cm^{-1} is attributed to C–H stretching vibrations. The absorption bands in the ranges of 1435–1232 cm^{-1} and 1057–610 cm^{-1} are associated with asymmetric C–O–C stretching vibrations and β-1,4-glycosidic

linkages between glucose units in the cellulose structure. After the carboxymethylation process, water hyacinth cellulose was successfully converted into Na-CMC NPs. A comparison between cellulose and Na-CMC NPs reveals similar wavenumbers at approximately 1651 cm^{-1} and 1442 cm^{-1}, however, the absorption intensity differs significantly. Cellulose exhibits weak absorption at these wavenumbers, whereas Na-CMC NPs show strong and sharp absorption bands. The prominent absorption bands in the range of 1651–1442 cm^{-1} confirm the presence of carboxylate (COO^-) groups, indicating successful carboxymethylation of the cellulose. Notably, transmittance peaks were detected at 3424 cm^{-1} and 1422.24 cm^{-1}, with minor shifts in peak positions attributed to varying levels of pollutant contamination [21, 32, 35]. These peaks correspond to several vibrational groups, including CH_2–, C–OH, C–C and C–O and –OH [36]. Joyline explained the peak shifts observed in the FTIR spectrum of the extracted Na-CMC NPs from E-crassipes, attributing this phenomenon to a heightened tendency for saline absorption [37]. The presence of absorbed water causes CMC to transform into a gel-like material. This property makes the present Na-CMC NPs substance is a superabsorbent polymer. Many authors have reported the structural characteristic of Na-CMC NPs [32, 36–43]. The FTIR spectrum yields essential insights into the altered chemical structure of (CMC) derived from water hyacinth. A broad band appearing at approximately 3422 cm^{-1} is indicative of O–H stretching vibrations, while a peak around 2915 cm^{-1} corresponds to C–H stretching vibrations. Additionally, the peak recorded at 1631.65 cm^{-1} is associated with CH–O–CH_2 stretching vibrations [32]. These vibration patterns represent defining features of both Na-CMC NPs and cellulose [32]. A careful examination of the obtained FTIR spectrum reveals the absence of two prominent bands at 1510 cm^{-1} and 1255.70 cm^{-1}, confirms the substantial removal of lignin. The peak observed around 1608 cm^{-1} signifies the presence of a carbonyl group (C=O), while the peak near 1422 cm^{-1} is indicative of methyl (CH_3) groups. These findings confirm that the extracted sample from water hyacinth is indeed (Na-CMC) NPs. Furthermore, carboxyl groups in salt form typically exhibit wave number bands ranging from 1640–1460 cm^{-1} to (1400–1450) cm^{-1} [44]. Bands within ranges of (1435–1232) cm^{-1} and 1057–610 cm^{-1} signify the asymmetric bridge stretching (C–O–C) of water hyacinth cellulose, as well as the glycosidic bonds connecting the glucose units in cellulose. These spectral features illustrate the transformation from cellulose to CMC through the carboxymethylation process. Both cellulose and CMC display peaks at similar wave numbers, such as 1651 cm^{-1} and 1442 cm^{-1} and confirms the presence of COO^- group. However, CMC demonstrates significantly stronger and sharper absorption at these wave numbers, which is indicative of successful carboxymethylation. The pronounced absorption band in the range of 1651–1442 cm^{-1} further confirms the presence of the COO^- group, underscoring the incorporation of carboxymethyl substituents. The previous studies at wave numbers of 1620.1 cm^{-1} and 1423.4 cm^{-1}, which were indicative of carboxymethyl substitution [28]. Additionally, the presence of carboxymethyl groups was confirmed in the ranges of (1600–1640) cm^{-1} and (1400–1450) cm^{-1}, aligning with the findings of the present study. In this study, the peaks corresponding to the carboxymethyl groups are identified at 1608.4 cm^{-1} and 1422.2 cm^{-1}, respectively. Minor variations observed at these wave numbers attributed to contamination of heavy metal impurities or due to combination bands influenced by the presence of water [21, 28, 32, 35].

Length and Strength of Hydrogen Bonds

Hydrogen bonding is significant due to its crucial role in various chemical, physical, and biochemical processes [44]. Determination of hydrogen bond and strength are essential for understanding of mechanical strength and flexibility of cellulosic material [45]. A hydrogen bond can be described as a scenario where a hydrogen atom, under specific conditions, is strongly attracted to two atoms, allowing it to function as a bond between them. Hydrogen bonds can be categorized into three types based on their strength: weak (4.18–16.74) kJ/mol., moderate (16.74–62.76) kJ/mol, and strong (62.74–166.154) kJ/mol [46]. Small change in bond length influences: water solubility, viscosity, rheology, thermal stability and mechanical flexibility [47]. Substances containing carboxylic groups tend to form molecular aggregates. This behavior is not limited to hydroxyl (OH) groups; it is also observed in molecules with NH and CH linkages. The strongest interactions are typically found between hydroxyl groups and oxygen atoms, whether in the same molecule (intramolecular interaction) or in different molecules (intermolecular interaction) [48]. The intermolecular bond is formed between two molecules due to the influence of electromagnetic forces of attraction or repulsion [49]. By utilizing the methodology developed by George Pimental and Charles H. Sederholm to determine the O–H…O distance (R) in hydrogen-bonded crystals, the infrared transmittance band associated with O–H stretching motion. The relationship between frequency shift (Δv) and bond distance is related in the following formula (4), [50, 51]:

$$R\,(\text{Å}) = 2.84 - (\Delta\nu/(4430)) \quad (4)$$

Both Hydrogen bond energy and length are key parameters when analyzing the molecular interaction in Na-CMC NPs and water hyacinth samples, particularly in structural modifications brought by carboxymethylation [35]. Increase H-Bonding energy leads to decrease crystallinity, increase the chain flexibility and enhance ionic conductivity [52]. Figure 4 shows the dependence of –O–H energy (E_H) of several –OH stretching bonds of hydrogen bond on the wavenumber value of the transmission peak of FTIR spectrum.

An inverse relationship between O–H bond distance and IR frequency transmission bands has been well-documented [50, 51, 53]. This correlation is significant in understanding the molecular interactions and structural dynamics. Determination hydrogen bond length in Na-CMC NPs is essential for, Based on the IR analysis results of the extracted (Na-CMC) NPs from *Eichhornia crassipes* (E-Crassipes), comparisons were made using the Wiley Database for IR polymers and monomers. The suggested molecular structure for this CMC sample was derived from the database entry titled "IR—Surfactants, Hummel – Wiley, Record ID 1016" [54].

Name Sodium carboxymethylcellulose;

Appearance White powder	Hummel Decimal Number 95561
Sample Description	Plasticizer, adhesive, thickener
Source of Sample	Hoechst AG, Frankfurt/Main, Germany
Molecular weight (M.W.): 250,000	DS = 0.64

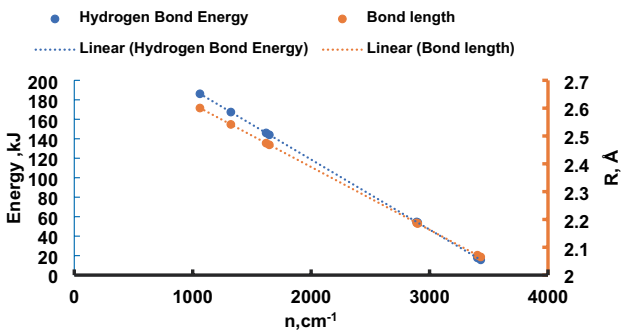


Fig. 4 The dependence of –O–H energy (E_H) of several –OH stretching, and bonds dependence of hydrogen bond length R, on the transmission peak frequency on the wavenumber value of the transmission peak of FTIR spectrum

NMR Result

Figure 5a shows a side-by-side comparison of the ^{1}H-NMR spectra for native cellulose and Na-CMC NPs. In the native cellulose spectrum, the main signals appear between 3.0 and 5.5 ppm, with a distinct peak near 4.8 ppm representing the anomeric proton. The Na-CMC NPs spectrum retains these backbone signals but also introduces new peaks in the 3.3–4.0 ppm region, which correspond to methylene protons from the carboxymethyl groups. These additional signals confirm that cellulose has been successfully carboxymethylated, while the presence of the original backbone peaks indicates that the polysaccharide structure remains intact [55]. Thus affirming the structural configurations illustrated in the NMR spectra, see Fig. 5b and Scheme 2. The ^{1}H-NMR spectrum of sodium carboxymethyl cellulose (Na-CMC) NPs clearly reflects the polymeric nature and chemical modification of cellulose. Most of the proton signals appear as a broad group of overlapping peaks in the region between δ 3.0 and 5.5 ppm, which is typical for polysaccharides. These resonances arise mainly from the protons of the glucose rings (H-2 to H-6) in the cellulose backbone. Because Na-CMC NPs is a substituted polymer with a non-uniform structure, these signals are broadened and partially overlap rather than appearing as sharp, well-defined peaks. The resonance observed around δ 4.5–5.2 ppm can be assigned to the anomeric proton (H-1) of the glucose units. Its broad shape reflects the loss of crystallinity and the variation in chemical environment caused by the introduction of carboxymethyl groups. In addition, signals in the δ 3.2–4.2 ppm region are attributed to the methylene protons (–CH_2–) of the carboxymethyl substituents. The appearance of these peaks confirms that carboxymethyl groups have been successfully introduced onto the cellulose backbone. The overlap and broadness of these resonances suggest that substitution occurs at different hydroxyl positions along the polymer chain. Importantly, the spectrum does not show noticeable peaks in the aliphatic region below δ 2.5 ppm or in the aromatic region above δ 6.0 ppm, indicating that the sample is free from significant low-molecular-weight impurities or aromatic contaminants. Overall, the spectral features are consistent with those expected for Na-CMC NPs and confirm the successful modification of cellulose [56]. The insert provides an enlarged view of a selected part of the ^{1}H-NMR spectrum, allowing a closer inspection of the overlapping proton signals. This zoomed-in region makes it easier to observe the anomeric proton and the methylene protons of the carboxymethyl groups, which are less clearly distinguished in the full spectrum. By magnifying this area, subtle differences in peak shape and intensity become more visible, highlighting the heterogeneous substitution pattern typical of Na-CMC NPs [57].

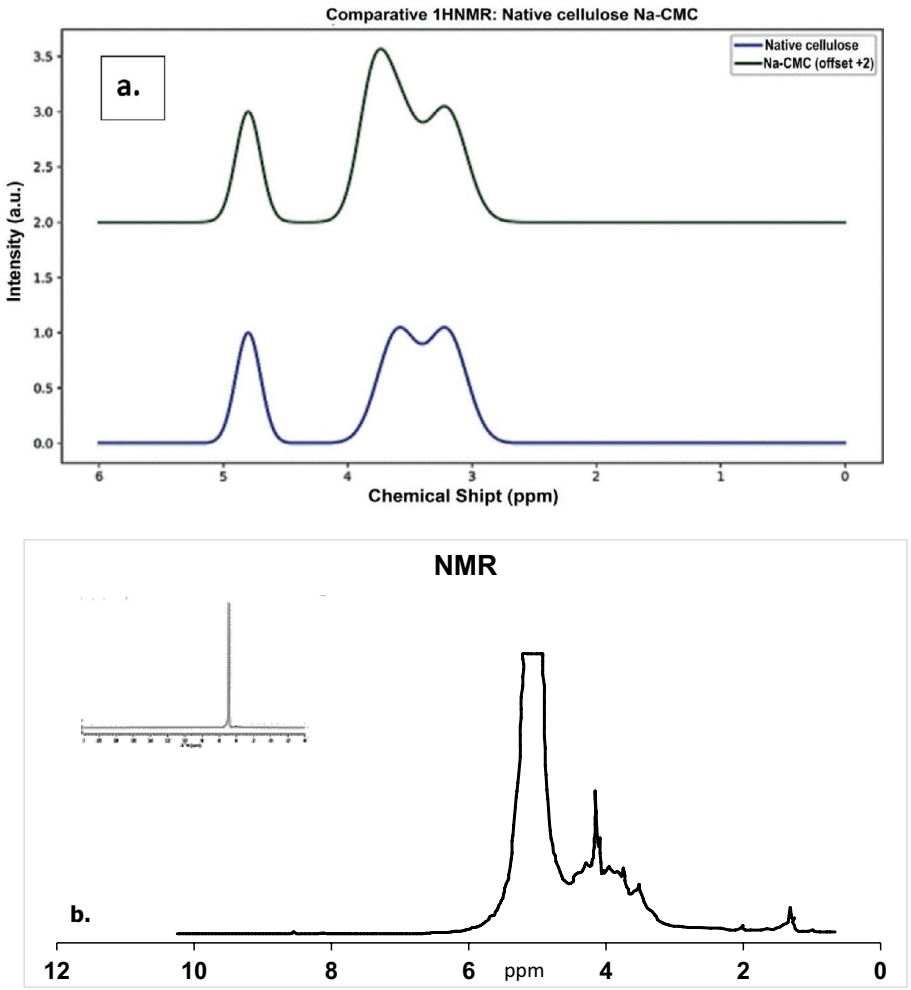
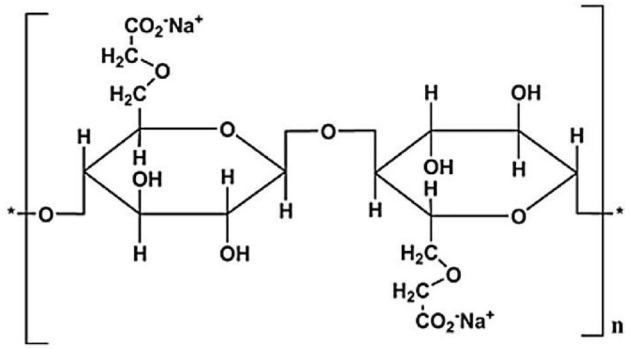


Fig. 5 **a** A side-by-side comparison of the ^{1}H NMR spectra for native cellulose and Na-CMC NPs. **b** NMR spectrograph of the extracted Na-CMC NPs from the stem of Hyacinth water, where (M.W.): 250,000 and ΔS = 0.64



Scheme 2 The proposed molecular structure of the extracted of (Na-CMC) NPs

In conclusion, taken together, the XRD, FTIR, and NMR results provide consistent and complementary evidence for the successful conversion of water hyacinth cellulose into sodium carboxymethylcellulose nanoparticles. XRD demonstrates disruption of crystalline order, FTIR confirms the formation of carboxylate functional groups, and NMR verifies the incorporation of carboxymethyl units into the cellulose backbone. These findings establish that the synthesis process achieves effective chemical modification while preserving the fundamental polysaccharide structure, which is essential for the observed thermal and dielectric behavior discussed in subsequent sections. FTIR confirms the chemical modification through the appearance of strong bands at 1651–1442 cm^{-1} assigned to carboxylate ($–COO^{–}$) groups, while the characteristic cellulose bands remain, indicating preservation of the polysaccharide backbone. The ^{1}H NMR spectra support this conclusion by showing new resonances in the δ 3.2–4.2 ppm region corresponding to methylene protons ($–CH_2–$) of the carboxymethyl substituents, together with the original glucose proton signals. XRD shows a reduction in crystalline order after modification, reflecting disruption of the hydrogen-bonding network between cellulose chains. Thus, XRD demonstrates structural disordering, FTIR verifies functional group formation, and NMR confirms molecular incorporation of carboxymethyl groups. Together, these results provide consistent and direct evidence of successful Na-CMC synthesis.

Thermal Analysis

The Differential Thermal Scanning Calorimetry (DSC) Results

Differential thermal Scanning Calorimetry (DSC) measurements were performed within the temperature range of 236 K to 411 K, using a heating rate of 5 °C/min. The results, illustrated in Fig. 6, reveal several thermal transitions that are characteristic of (Na-CMC) NPs, a polysaccharide material known for its unique thermal properties.

Figure 6 illustrates a broad endothermic kink that begins at 285 ± 2 K, ends at 401 ± 2 K, and reaches its trough at around 352 ± 2 K, with an enthalpy value of 22 J/g. The minimum of the kink defined the glass transition temperature T_g = 352 K. Polysaccharides, such as CMC, exhibit strong water-binding properties due to their macromolecular structure, which is inherently disordered in the solid state and capable of undergoing hydration. The hydration dynamics depend on both the primary and supramolecular structures of the material. The observed endothermic kink at 285 K is primarily associated with water evaporation. This phase reflects significant physical and molecular changes occurring during the processes of N-deacetylation and carboxymethylation [54].

Furthermore, a narrow and sharp exothermic peak appears at 271 K, which is attributed to the decomposition of highly substituted polysaccharide regions within the Na-CMC NPs structure, as shown in the insert of Fig. 6; with enthalpy of 0.12 J/gm.

Thermogravimetric Analysis (TGA)

Thermogravimetric analysis (TGA) is an analytical technique used to measure changes in the mass of a material as a function of temperature and time [58]. This method is essential for investigating various thermal phenomena, including sublimation, vaporization, absorption, adsorption, and desorption, as the temperature increases [59]. TGA results

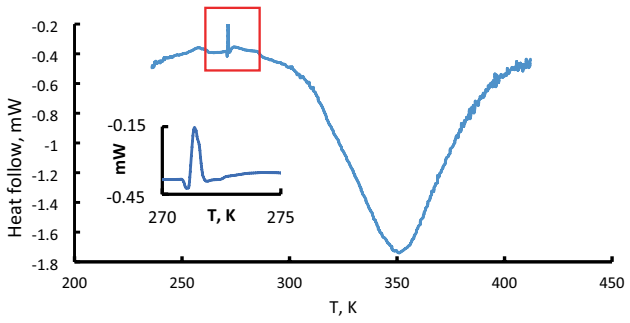


Fig. 6 DSC performed in the temperature range 236 K up to 411 K. The insert of Fig. (6) shows enlarged scale in the temperature range 270 K up to 275 K

are typically presented in one of two forms, I-Weight Loss vs. Temperature; which tracks the material's weight reduction as it is heated and II-Derivative Thermogravimetric Analysis (DrTGA); which represents the rate of weight loss with respect to temperature, offering insights into distinct stages of material degradation.

Figure 7a and b illustrate the thermogravimetric analysis (TGA) and derivative thermogravimetric analysis (DrTGA) of (Na-CMC) NPs, clarifying the dependence of mass loss and weight loss rate on temperature. The inset in Fig. 7a indicates that the increase in the α value commences at 1203 K, peaks at 1227 K, and subsequently begins to decline. The helical structure of Na-CMC NPs facilitates the interaction of its hydroxyl (H–O) groups with the surface [52].

Figure 7a reveals a series of decomposition events, each corresponding to specific stages of weight loss: First Decomposition Stage: Begins at 373 ± 1 K, reaching a plateau at 464 ± 1 K, and is associated with minimal weight loss. Second Decomposition Stage: Commences at 526 ± 1 K, stabilizing at a plateau of 565 ± 1 K, with a weight loss of 12.8%. Third Decomposition Stage: Onset occurs at 852 ± 1 K, concluding at 892 ± 1 K, followed by a substantial weight loss of 38%. Final Decomposition Stage: Initiates at 1077 ± 1 K, culminating in a plateau at 1180 ± 1 K, accompanied by a significant weight loss of 45%. The sequential decomposition events in Fig. 7a reflect the existence of distinct stages of material degradation, each characterized by unique kinetics.

Figure 7b illustrates the relationship between the rate of mass loss (DrTGA) and the decomposition of Na-CMC NPs over time, recorded at a constant heating rate of 10 °C/min. Four distinct minima are identified at temperatures of 351 K, 554 K, 856 K, and 1160 K. These minima correspond to the midpoints of the mass-loss events depicted in Fig. 7a and b. Drawing on the research of Basta [60], such minima in the DrTGA curve are attributed to the evaporation of moisture or the vaporization of specific components within the adhesive polymer blend. Furthermore, the observed low rate of mass loss as the temperature increases underscores the remarkable thermal stability of sodium carboxymethyl cellulose derived from the stem of (E-Crassipes).

Kinetics of Thermal Decomposition

Using change in sample mass as a function of increasing temperature is a well-established method for determining the kinetics of thermal decomposition [34, 60–62]. Thermogravimetric analysis (TGA) is employed to record the data associated with this mass change as temperature rises. The resulting data is then analyzed using the formulas proposed by Coats and Friedman [63–65].

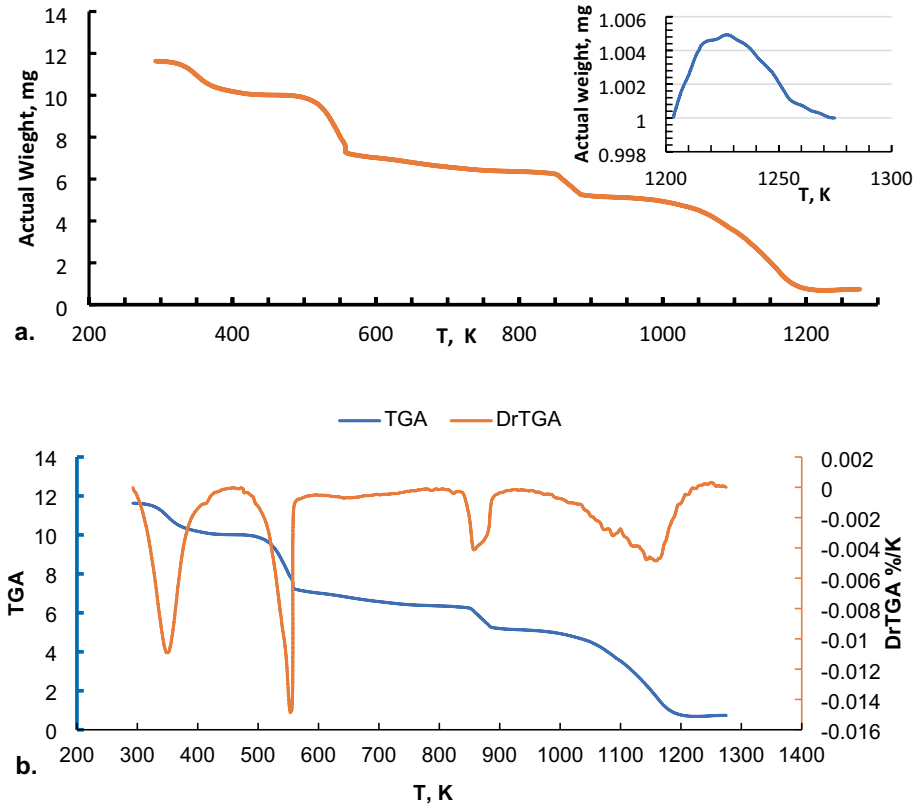


Fig. 7 **a** Shows the dependence of mass loss on temperature. **b** Relationship between TGA and DrTGA (rate of mass loss) of Na-CMC NPs as a function of temperature at a constant heating rate of 10 °C/min

Table 2 The energy of decomposition, degradation frequency (A), and the reaction order

W. Coats and J. P. Redfern, Method [48]				A. Broido Method [51]					
Temperature range, K	Ea, kJ/mole	R^2	N	Ea, kJ/mole	A, Hz	R^2	T_m, K	Δm	Δm%
(326–386) 1st Stage	4.9	0.9907	3	26.123	8.37	0.9488	351	1.34	11.54
(512–565) 2nd Stage	387.3	0.9988	3	0.705	152	0.9516	554	5.34	46
(581–622) 3rd Stage	62.7	0.9996	2.5	106.3	0.27	0.9999	584	6.42	55
(718–910) 4th Stage	0.079	0.9287	2	18.84	0.65	0.9287	858	10.68	92

$$Log10\left(\frac{(1-(1-\alpha)^{1-n}}{T^2(1-n)}\right) = Log10\frac{AR}{aE}\left(1-\frac{2RT}{E}\right) - \frac{E}{2.3RT} \quad (5)$$

By Plotting $\ln[(\frac{1}{(1-\alpha)})]$ versus 1/T, the line with slope = E_a /R and intercept = $\ln[(\frac{R}{E_a})(\frac{A}{\beta})T_m^2$ where: (α) represents fractional conversion $\alpha = \frac{m_i - m_\alpha}{m_i - m_F}$; ($m_i$) denotes the initial sample mass at the onset of the reaction, while (m_f) signifies the sample mass at the end of the reaction and, m_α is mass during the degradation process [66, 67]. Additionally, (n) indicates the order of the degradation reaction corresponding to the maximum correlation factor (R^2), T is the absolute temperature measured in Kelvin, (A) represents the reaction frequency, a corresponds to the heating rate, and (R) is the universal gas constant, and (E) symbolizes the energy associated with decomposition. From the relationships established in the preceding equations, a straight line can be derived with a slope given by s = E/(2.3R) and an intercept that must be calculated. The energy of decomposition, degradation frequency (A), and the reaction order are determined as shown in Table 2, which presents the kinetic parameters for decomposition. Here, n is identified as the order of decomposition. The parameter A reflects the frequency of the reaction, while Δm represents the difference between the initial and final sample masses. T_m indicates the temperature at which the rate of mass loss reaches its peak, and Δm% quantifies the ratio of mass loss relative to the initial sample mass. Table 2 kinetic parameters of decomposition where n is the decomposition order, A is the frequency and Δm is the difference between the sample starting mass and the sample final mass. T_m is the temperature of maximum mass lose rate, and Δm% is the ratio between the mass loss and the initial sample mass. The obtained results of activation energy of degradation from the two methods are not matches. The degradation process of carboxymethyl cellulose–copper complexes was thoroughly examined by Nashar et al. [65]. Utilizing the Coats and Redfern equations [68] to determine degradation kinetic parameters, the activation energy values listed in Table 2 were found to align closely with those reported by Nelson et al. [69]. The first degradation stage of CMC, observed at a heating rate

of 10 min/°C, is attributed to the evaporation of adsorbed moisture and the degradation of impurities [64]. The second degradation stage occurs within the temperature range of (215–565) K and is associated with the dehydration of CMC, a process that generates CO_2 and CO as byproducts [66]. The third degradation stage (718–910) K likely corresponds to the breakdown of products formed during earlier heating stages [66].

Dielectric Permittivity Measurements

Thermal Dependence of Dielectric Permittivity

Figure 8a illustrates that the dielectric constant behavior as ln(ε′) versus temperature, at different selected frequencies. This figure shows an increasing trend with temperature, reaching a peak at 314 K before undergoing a decline and eventually stabilizing at 343 K. This behavior correlates with the broad thermal transition evident in the differential scanning calorimetry (DSC) results presented in (Fig. 6), where a notable inflection point emerges at 300 K and extends to 411 K. The observed shift in temperature between the onset and endpoints of the ε′ and DSC curves can be attributed to variations in the heating rates applied during the two measurement techniques. Given that the thermal properties of (CMC) are indeed heating-rate-dependent [64]. This discrepancy is attributed to reduced thermal stability of CMC at elevated temperatures [70]. Notably, a subtle kink emerges starting at 384 K, persisting across all tested frequencies. This kink corresponds with the onset of the first decomposition stage of (CMC), as evidenced by the thermal analysis presented in Fig. 7a and b. The arrow in Fig. 8a points out to kink at 384 K. This transition is close to the end of the first degradation stage 386 K, as shown in Table 2. Figure 8a also demonstrates that the dielectric constant (ε′) experiences a decline as frequency increases, ultimately stabilizing at 352 K. Remarkably, this temperature coincides with the minimum point of the kink observed in the differential scanning calorimetry (DSC) curve (Fig. 6). The observed decrease in ε′ with rising temperature is intricately associated with orientational polarization, which dictates the thermal motion of molecules. As the temperature escalates, the influx of thermal energy disrupts the orderly alignment of polar molecules, thereby reducing their capacity to reorient in response to an applied electric field [70,

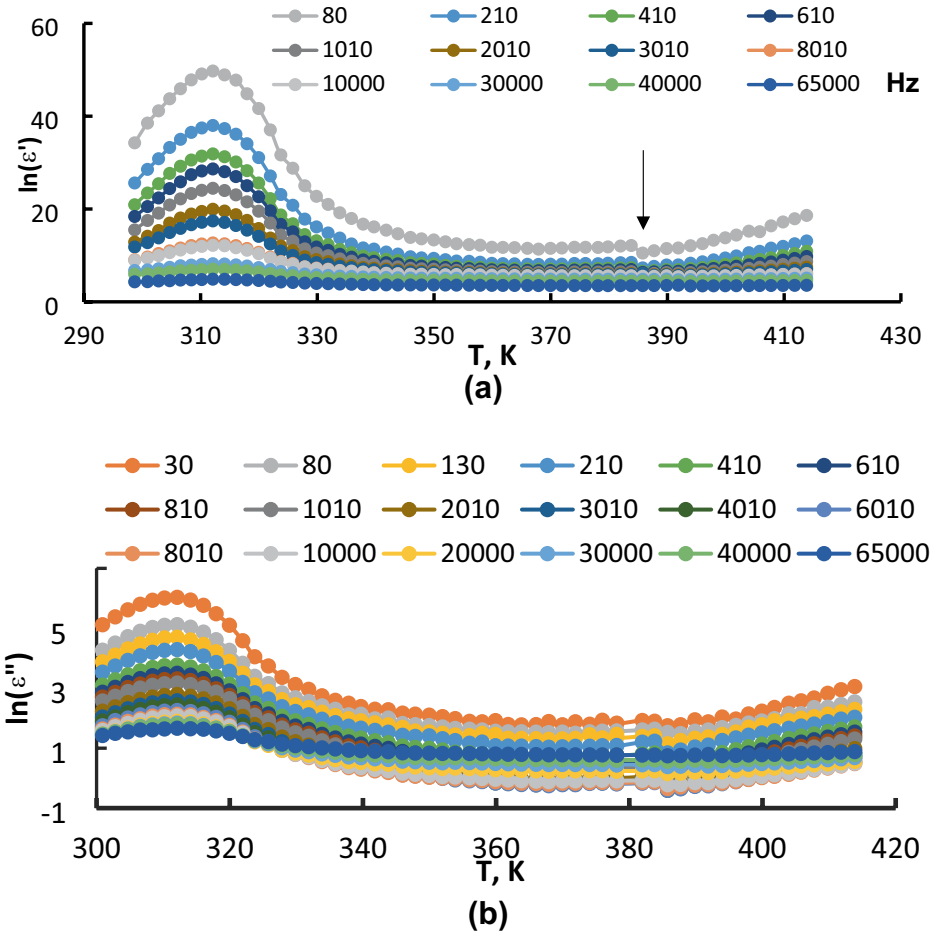


Fig. 8 **a** Temperature dependence of real part of dielectric constant ε' at selected frequencies. **b** The dependence of the dielectric loss ln (ε") on temperature at different selected frequencies

71]. The dielectric anomaly observed can be attributed to the structural and compositional changes occurring in CMC during decomposition, which likely involve bond cleavage or reorganization of the polymer matrix. The relaxation time is intricately linked to various polarization mechanisms namely electronic, atomic, dipolar, space charge, and interfacial polarization which are influenced by the composition and structural characteristics of the material (such as organic versus inorganic and crystalline versus amorphous) [72].

Figure 8b shows the dependence of the dielectric loss ln (ε'') on temperature at different selected frequencies. The behavior of dielectric loss as a function of temperature confirms the correlation between thermal behavior and the dielectric behavior. This figure shows an increasing trend with temperature, reaching a peak at 314 K before undergoing a decline and eventually stabilizing at 343 K. This phenomenon aligns with the broad thermal transition evident in the differential scanning calorimetry (DSC) results presented in Fig. 6, where a notable inflection point emerges at 300 K and extends to 411 K. The observed shift in temperature between the onset and endpoints of the ε′, ε'' and DSC curves can be attributed to variations in the heating rates applied during the two measurement techniques. Also, in ε''=F (T) a subtle kink emerges starting at 384 K, persisting across all tested frequencies. This kink corresponds with the onset of the first decomposition stage of (CMC), as evidenced by the thermal degradation analysis.

Frequency Dependence of Dielectric Permittivity

Figure 9a and b demonstrate the frequency dependent behavior of the dielectric constant (ε') and dielectric loss (ε"). At low frequencies, both ε' and ε" diverge, decreasing with rising temperature, while they converge at high frequencies. The observed reduction in ε' and ε" with increasing temperature can be attributed to the following factors:

Dipole Disruption: Elevated temperatures increase molecular mobility, disrupting the alignment of dipoles under an applied electric field. This reduces the material's ability to polarize effectively, lowering ε' [70, 73].
Phase Transitions: Thermal transitions (e.g., solid-to-gel) may weaken intermolecular interactions in (CMC), compromising structural integrity and polarization efficiency.
Moisture Loss: Although higher temperatures enhance ionic mobility, excessive thermal energy can dissociate or evaporate bound moisture in the CMC matrix. Reduction of water content diminishes charge carrier concentration, further decreasing ε' and ε".
Water-State Alteration: Temperature-induced changes in water interactions (e.g., bound-to-free transitions or evaporation) can destabilize dielectric properties [74–76].

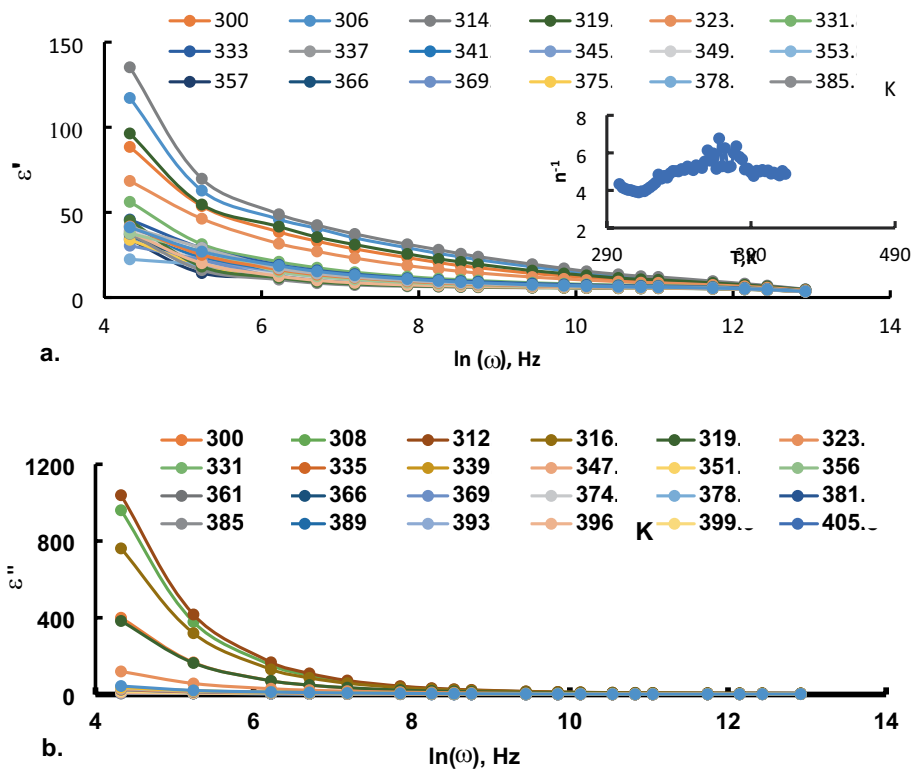


Fig. 9 **a** Frequency dependence of real part of dielectric constant ε' at different temperatures. Insert of Fig. (9a) shows the exponent (n^{-1}) versus temperature, revealing a power-law relationship ($\varepsilon' \propto \omega^{n-1}$). **b** Shows Frequency dependence of (ε'') at different selected temperatures

Figure 9a presents a plot of (ε') against frequency, which reveals a power-law relationship ($\varepsilon' \propto \omega^{\wedge}(n^{-1})$) [66]. Fluctuations in the exponent (n^{-1}) correlate with thermogravimetric analysis (TGA) data. The emergence of a hump and the variability in n-value around 351 K correspond to the second decomposition stage shown in Fig. 7b (T ~ 354 K). This correlation highlights the interconnectedness of dielectric behavior and thermal degradation processes in carboxymethyl cellulose (CMC). Notably, fluctuations in the exponent (n^{-1}) align with TGA data: the onset of a hump and n-value variability at 351 K corresponds to the second decomposition stage observed in Fig. 7b (starting at 354 K). This correlation underscores the interdependence of dielectric behavior and thermal degradation processes in CMC.

Figure 9b shows similar frequency dependence of (ε") as observed for (ε'). At low frequencies, the increases in both the real (ε') and imaginary (ε") parts of the permittivity with temperature are attributed to a shift in dielectric relaxation processes to higher frequencies, as enhanced thermal energy facilitates ionic hopping and diffusion, which increases the mobility of both sodium counter-ions (Na^+) and the rotational freedom of polar -COO^- groups along the polymer backbone [69]. Conversely, the convergence at high frequencies indicates a limit to these dipole and ionic contributions at short timescales. The persistent low-frequency divergence, however, is attributed to interfacial polarization (Maxwell–Wagner–Sillars effect) arising from the accumulation of mobile Na^+ ions at internal boundaries within the heterogeneous polymer matrix, such as between regions of differing crystallinity or hydration [77].

The dielectric behavior of (Na-CMC) NPs is of fundamental importance due to its direct link to the polymer's unique ion dipole interactions and hydration dynamics. As a water soluble polyelectrolyte, the sample's dielectric constant and loss are highly dependent on frequency, moisture content, and ion mobility. At low frequencies, the high dielectric constant arises from the orientation of its polar -COO^-Na^+ groups and bound water molecules, which is critical for its charge storage capability. This strong polarization enables its primary use as a high performance, bio-based thickener and stabilizer in foods and pharmaceuticals, where dielectric properties govern viscous structuring and colloidal interactions.

Furthermore, the dielectric relaxation spectra reveal crucial information about segmental motion and ionic conduction, which dictates performance in advanced applications. In solid polymer electrolytes for biodegradable electronics, sample moderate ionic conductivity and dielectric stability are key for facilitating ion transport. In biomedical contexts like hydrogel wound dressings or tissue scaffolds, its dielectric response influences cell adhesion and drug release kinetics by modulating local polarity and swelling behavior. Therefore, understanding and tailoring Na-CMC's dielectric properties is essential for optimizing its functionality across industries from controlling rheology in consumer products to enabling next generation sustainable materials.

Dielectric Modulus

Electrode polarization leads to a notable dispersion in the frequency dependence of permittivity. To mitigate the effects of electrode polarization, Macedo et al. [77] proposed using the dielectric modulus as a corrective measure. They introduced the concept of the dielectric modulus, defined as $M^* = 1/\varepsilon^*$ where ε^* represents the complex permittivity expressed as $\varepsilon^* = \varepsilon' + i\varepsilon''$. This formulation effectively addresses the challenges posed by electrode polarization, enabling a more accurate analysis of the dielectric properties of materials.

$$M' = \frac{1}{\varepsilon'(1+\tan^2\delta)}, \quad M'' = \frac{i\tan\delta}{\varepsilon'(1+\tan^2\delta)} \tag{6}$$

Figure 10a elucidates the relationship between the real component of the dielectric modulus (M') and frequency across various selected temperatures. Notably, this depiction deliberately omits the effects of electrode polarization. At elevated frequencies, permittivity is predominantly influenced by instantaneous electronic and atomic polarizations. This underscores the critical importance of analyzing dielectric modulus to circumvent artifacts introduced by electrode polarization. Conversely, Fig. 10b illustrates the behavior of the imaginary component of the dielectric modulus (M") as a function of frequency for different temperature conditions. The observed increase in M' with rising frequency can be attributed to the constrained mobility of charge carriers over short distances. Furthermore, the manifestation of an asymmetric semicircular arc in the low-frequency region serves as evidence for the presence of electrical relaxation phenomena. This behavior is particularly pronounced in the Sodium carboxymethyl cellulose samples investigated, corroborating the findings documented in [78, 79]. Figure 10a and b show features of ionic conductivity, namely S shape of M' dispersion and M" peak. It is noted that the peak of M" shifts its position as frequency changes, but the amplitude not changes with changing temperature. Figure 11a clarify the peak shift of ln(M"). The peak max frequency values are plotted as function of temperature shown in Fig. 11b. The relaxation can be analyzed using Equation:

$$f = f_o e \frac{-E_a}{KT} \tag{7}$$

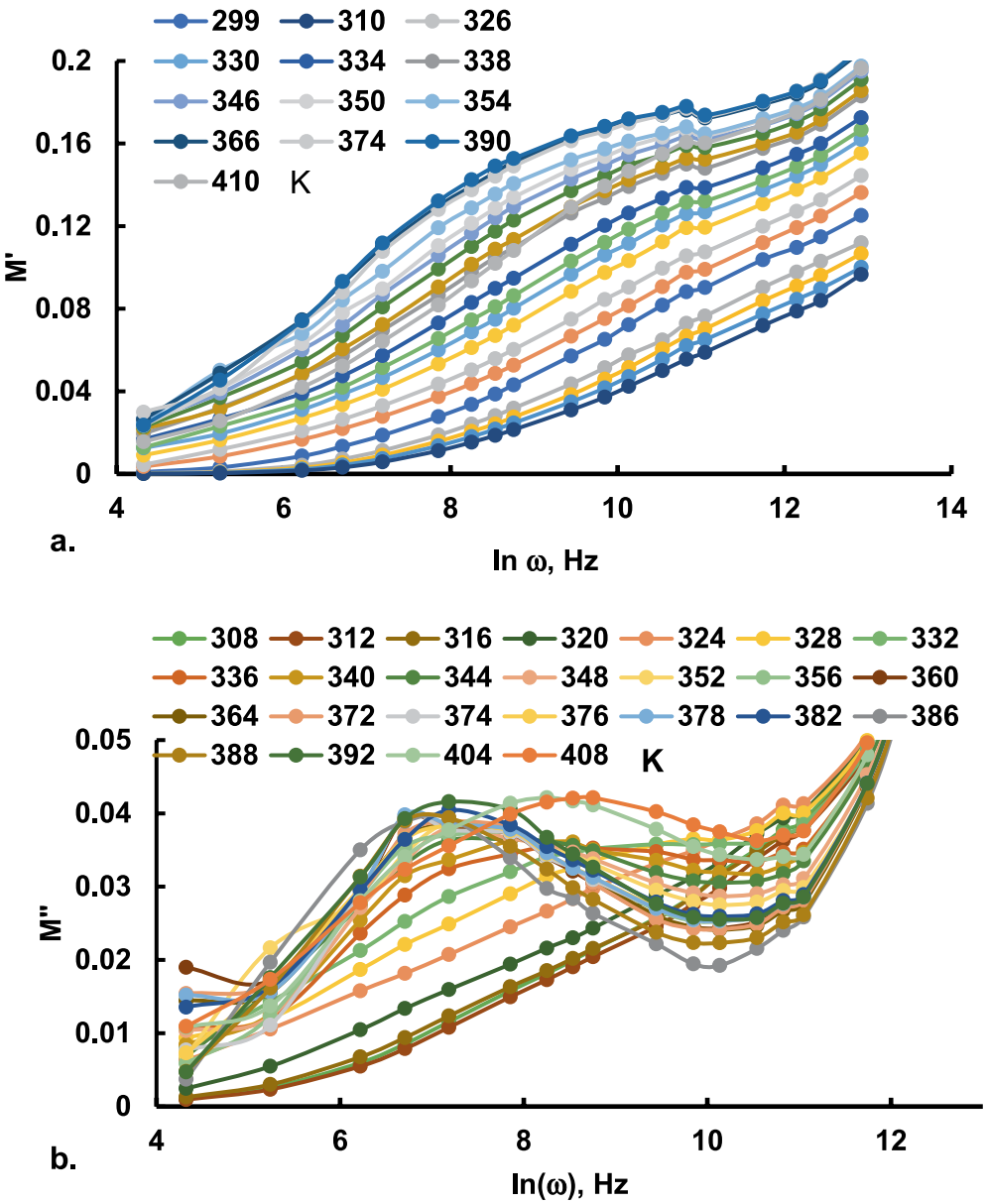
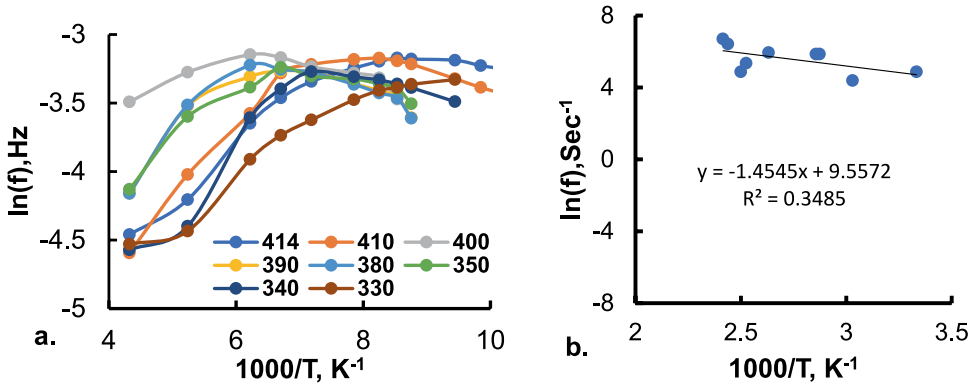


Fig. 10 **a** Frequency dependence of (M') at different selected temperatures. **b** Frequency dependence of (M'') at different selected temperatures

Fig. 11 **a** Shows the peak shift ln (M'') versus temperature as 1000/T. **b** Shows the peak max frequency values as function of 1000/T



where E_a is the relaxation activation energy which yields, $E_a = 0.125$ eV, $f_o = 14{,}146$ Hz.

Conductivity Measurements

Temperature Dependence of A. C. Conductivity

Figure 12a illustrates the dependence of σ_T on reciprocal temperature over the range of 300 K to 414 K. The conductivity profile shows distinct behavior across four regions:

Region I (300 K–312 K): Conductivity increases with rising temperature, indicating thermally activated processes.
Region II (314 K–330 K): A marked decrease in conductivity with increasing temperature suggests metallic-like behavior.
Region III (330 K–386 K): Conductivity decreases more smoothly with temperature, reflecting a transitional phase.
Region IV (386 K–414 K): Conductivity increases once again, displaying semiconductor-like behavior.

These divergences are observable across all frequencies up to 8010 Hz and remain slightly visible between 20 and 65 kHz. Such detailed analysis of σ_T provides valuable insights into the temperature-dependent conductivity mechanisms of the material.

Figure 12b illustrates the total electrical conductivity within the temperature range of 298 K to 312 K. Meanwhile, Fig. 12c depicts the relationship between the conduction activation energy Δ E and $\ln(\sigma_{dc})$ as a function of temperature within the same range. The observed decrease in activation energy, coupled with the increase in $\ln(\sigma_{dc})$ with temperature, supports the characterization of sodium carboxymethylcellulose as a semiconductor in the temperature span of 298 K to 312 K.

The data presented in Fig. 12d and e indicate that within the temperature range of 314 K to 330 K, conductivity decreases as temperature increases, while activation energy rises with temperature. The intermediate region (314–330 K) showed a complex, non-Arrhenius behavior which may be attributed to the interplay between ionic conduction from residual moisture/ions and the polymer's segmental motion, rather than metallic conduction. This interpretation aligns better with the polysaccharide nature of the material [23]. The term "metallic-like" for polysaccharide materials is a technically accurate shorthand for describing a state where chemical doping or nano-engineering induces. A negative dielectric constant in the IR, leading to high IR reflectivity. This makes them promising for sustainable flexible electronics, heat management (IR reflectors), electromagnetic interference (EMI) shielding, and optical coatings, all applications traditionally reserved for metals. The justification lies firmly in their measurable optical and electronic properties, which mirror those of metals in a specific, useful spectral range [85–87]. A comparison of metallic like polymer with true metallic behavior is illustrated in Table 3.

FTIR and NMR analyses demonstrate the presence of hydroxyl groups and moisture, as the extracted Na-CMC NPs material exhibits hydrophobic characteristics. In the temperature range of 330 K to 386 K, the adsorbed moisture begins to evaporate, and the conductivity is attributed to the melting of free crystalline water within the hydrogel [80]. The data presented in Fig. 12a indicate that within the temperature range of 386 K to 441 K, the conductivity of the material exhibits an increase corresponding to rising temperatures, characteristic of semiconductor behavior. In the temperature interval of 373 K to 433 K, the breaking of hydrogen bonds leads to the formation of hydroperoxide groups, which subsequently results in the depolarization of cellulose. Furthermore, carboxymethyl cellulose undergoes dissociation between 473 and 523 K. This dissociation contributes to the metallic behavior observed in phases (II) and (III) as depicted in Fig. 12a, which is attributed to the presence of hydroxyl groups (–OH) that enhance the electrical conductivity of (Na CMC) NPs. Thus, this phenomenon accounts for the metallic conductivity behavior observed in the temperature range of 386 K to 414 K [81–83]. Conversely, in both temperature regions (I) and (IV), the Arrhenius relationship is upheld. The frequency-dependent activation energy for both regions exhibits a strong correlation with the fitting equation:

$$\Delta E = \Delta E_a[1 - \exp\left(\frac{f}{f_i}\right)]^{\alpha} \tag{8}$$

where ΔE_a is the activation energy in low frequency limit and α is a constant with values ($0 < \alpha < 1.0$). Figure 13 shows the activation energy (ΔE) values (dots) and its variation with frequency (line) according to Eq. (8). The activation energy is found to decrease with increasing frequency for both phases but with attitude. Activation energy $\Delta E = (0.5$ eV–0.6 eV) for low frequencies can be associated with migration of chloride ion for both phases [82]. The low temperature phase, phase (I), shows parameters values of $\Delta E_a = 0.59$ eV, $f_a = 50.22$ Hz and $\alpha = 0.14$, while foe high temperature phase (IV); $\Delta E_a = 0.49$ eV, $f_a = 5.87$ kHz.

Frequency Dependence of Conductivity

Figure 14a shows ac conductivity, $\sigma_{aC} = \sigma_T - \sigma_{dc} = A(T)\omega^{s(T)}$, this figure shows that σ_{AC}

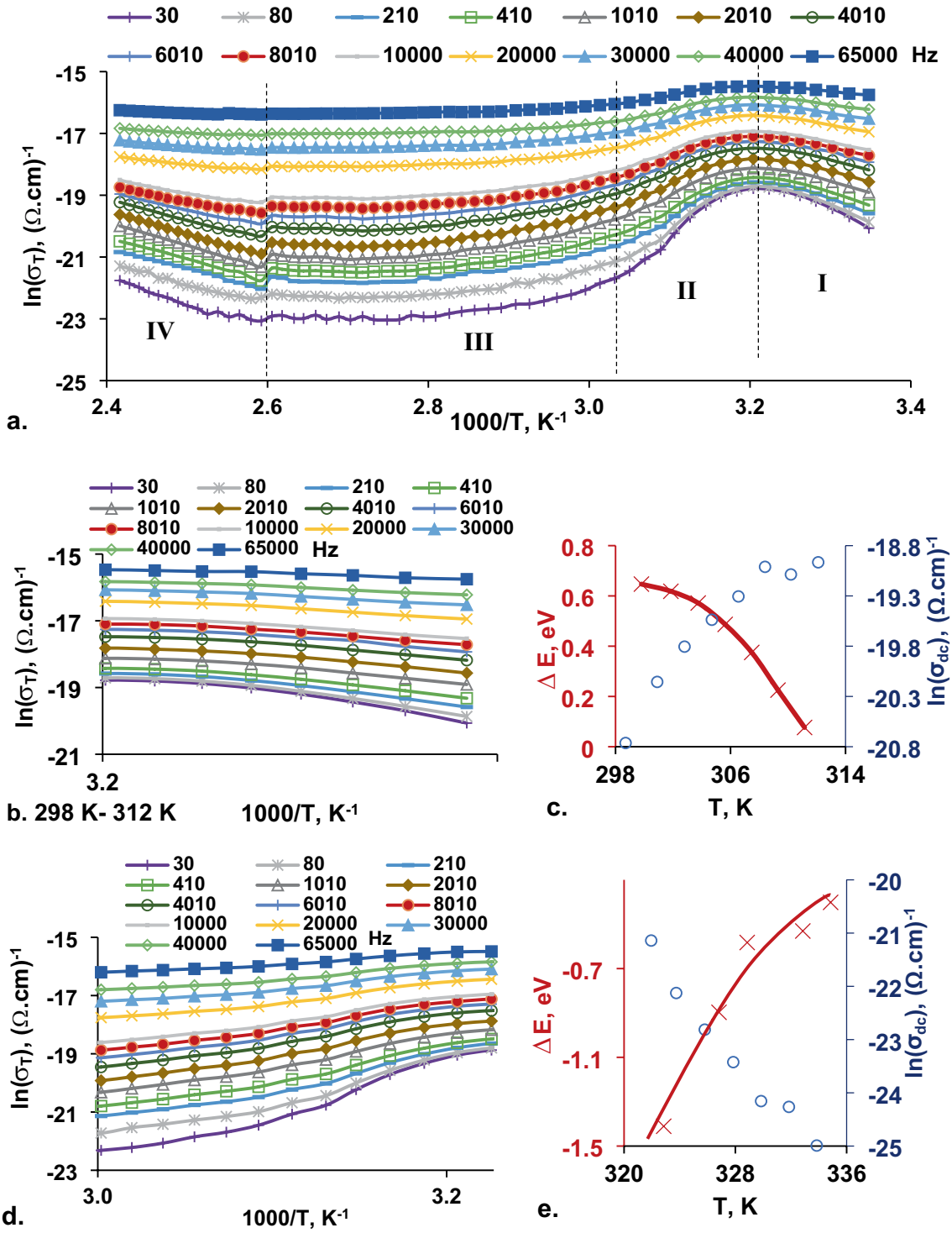


Fig. 12 **a** Illustrates the dependence of σT on reciprocal temperature over the range of 300 K to 414 K. **b** Show the dependence of conductivity on temperature in range (298–312) K. **c** Show the dependence of dc- conductivity and conduction activation energy on temperature. **d** Dependence of conductivity on reciprocal temperature in temperature range 314–330 K. **e** Dependence of both ln (σ_{dc}) and electric activation energy (ΔE) on temperature in the range (314 K–330 K)

Table 3 A comparison of metallic like polymer with true metallic behavior

Feature	True Metal (e.g., Copper)	Metallic-Like Polysaccharide Film	Justification
Primary Charge Carrier	Delocalized electrons	Holes (polarons), ions, or electrons in a composite	Different carrier, similar effect on collective oscillation
DC Conductivity	Very high (~10^6 S/cm)	Moderate to High (10^{-3} to 10^3 S/cm)	Can approach the lower end of metal conductivity
Key Optical Property	High reflectivity across VIS & IR	High IR reflectivity / low IR transmittance	The core of the "metallic-like" claim. Measurable via FTIR
Dielectric Constant (ε_1)	Negative in VIS/IR	Negative in the IR region	Mathematical proof of metal-like optical behavior
Mechanism	Sea of free electrons	Chemically doped conjugated systems, or percolated conductive networks	Engineered functionality rather than intrinsic property

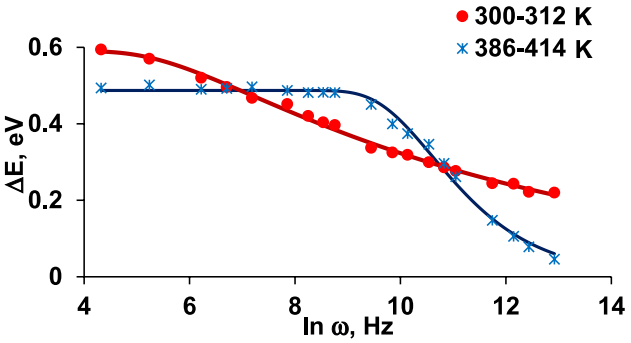


Fig. 13 Dependence of electric activation energy on frequency in temperature ranges (300 K–312 K), phase (I) and (386 K–414 K), phase (IV)

increase at all temperature measurement range as frequency increases but decreases with increasing temperature. The total conductivity σ_T follows the universal power law, where σ_{dc} is the direct current conductivity

$$\sigma_T = \sigma_{dc} + A(T)\omega^S \tag{9}$$

A(T) and s(T) are temperature dependent factors. where (0.5 < s < 1) as seen in Fig. 14b as proposed by Gargallo et al. [83] for ionic conductors.

Figure 14b show the dependence of exponent (s) and the intercept ln(A) of Eq. (9). The exponent s decreases from temperature 290 K up to 331 K after this temperature (s)

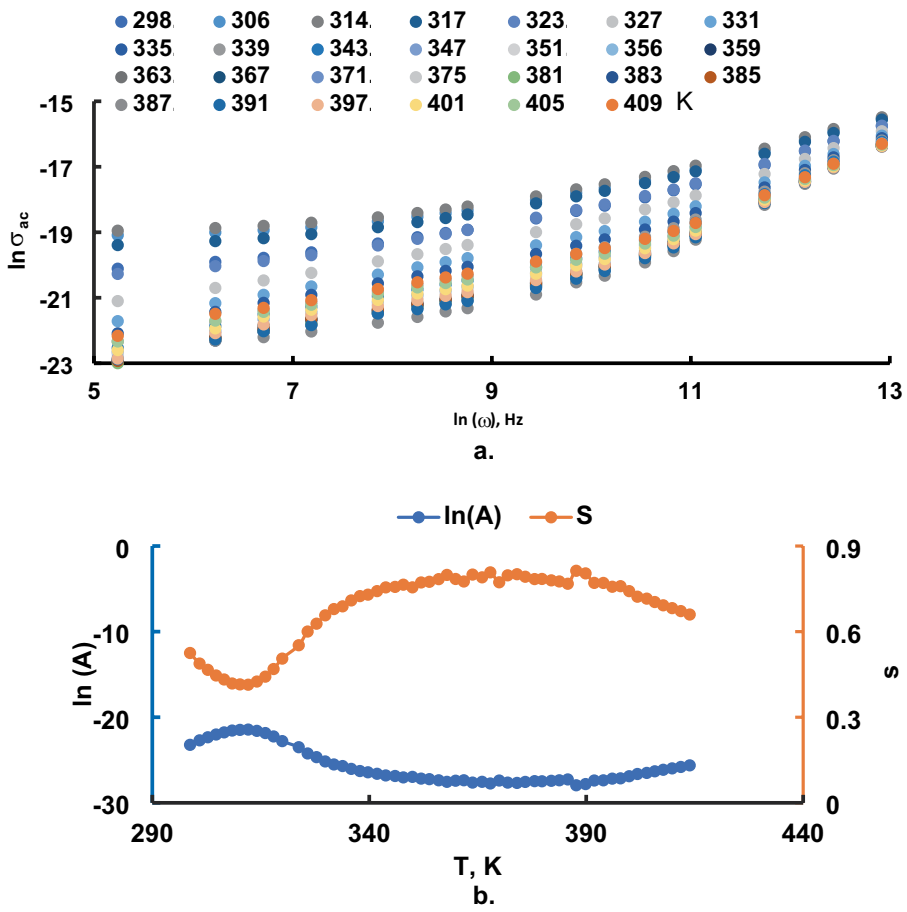


Fig. 14 **a** Dependence of AC conductivity on frequency. **b** Dependence of exponent (s) and intercept [ln (A)] on frequency

Table 4 Comparison of Thermogravimetric kinetic parameters of cellulose extracted from water hyacinth (E-crassipes) and cellulose extracted from different bio-originated sources

	Present kinetic results					He, M., et al. [12]				
	Temperature range; K	Ea, kJ/mol	Attributed to:	R^2	n	Cellulose Origin	Temperature range; K	Ea, kJ/mol	R	N
Cellulose from water hyacinth (Eichhornia) crassipes)	326–386, 1st stage	4.9	evaporation of adsorbed moisture	0.9907	3	Cotton Linters C. L	301.1–370.7 1st 447.8–515.2, 2nd	245.71 363.26	0.9939 0.9946	0.5 1.5
	(512–565), 2nd stage	378.3	Dehydration of CMC	0.9988	3	Viscose pulp (VP)	272.1–366.1 1st 371.7–509.6 2nd	238.4 95.86	0.9774 0.9847	0 0.5
	(581,622), 3rd stage	62.7	Breakdown products formed during earlier heating stages	0.9969	2.5	Micro crystalline cellulose (MC)	273.8–254.1 1st 447.8–522.4 2nd	245.71 363.55		
	(718–910), 4th stage	0.079		0.9287	2					

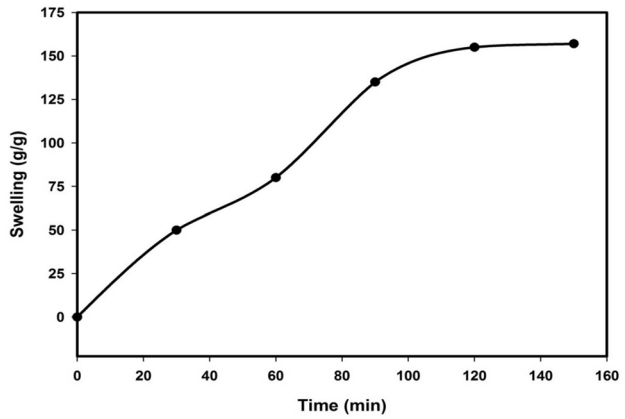


Fig. 15 Swelling in water of Na-CMC NPs hydrogel at 10 kGy

starts to increase but still less than 1 in this region hopping assist conduction by small polaron. At approximately 340 K, the exponent reaches a plateau that persists until 386 K before it starts to decline again [84]. This behavior of the exponent (s) versus temperature is the behavior proposed of the exponent (s) versus temperature in correlated barrier hopping (CBH) conduction mechanism [85]. The inverse behavior occurs at the same temperatures for the intercept ln(A) as shown in Fig. 14b.

Table 4 shows comparison of Thermogravimetric kinetic parameters of cellulose extracted from water hyacinth (E-crassipes) and cellulose extracted from different bio-originated sources like Cotton linters(CL), Viscose Pulp (VP) and microcrystalline cellulose (MC). Using Coats and Redfern method [12] the kinetic parameters determined; energy of decomposition Ea, reaction order n, and correlation factor R.

Applications

Hydrogels are cross-linked polymeric networks capable of absorbing substantial amounts of water and other liquids often up to hundreds of times their dry weight without dissolving, as observed in Na-CMC NPs hydrogel. The swelling ratio is an important parameter that reflects the degree of cross-linking within a polymer network [86]. Figure 15 illustrates the swelling behavior of Na-CMC NPs hydrogel in water, prepared using a constant gamma irradiation dose of 10 kGy. The swelling ratio increases markedly with time, reaching a maximum after approximately 120 min, at which point the Na-CMC NPs hydrogel absorbs nearly 155 times its own weight in water. This high swelling capacity is likely associated with the formation of a porous structure (Fig. 2b), which enhances water penetration and diffusion within the hydrogel network. Porosity facilitates rapid water transport through the polymer matrix. Moreover, the pronounced swelling behavior of the Na-CMC NPs hydrogel can be attributed to the presence of hydrophilic functional groups and sodium ions along the polymer chains, which promote efficient water absorption and retention. Owing to this high absorption capacity, Na-CMC NPs hydrogels show significant potential for various environmental, industrial, and medical applications, including the removal of heavy metals from contaminated water through adsorption and decontamination processes.

Conclusion

In this study, we investigated the structural, functional and electrical properties of water soluble processed polymer; Sodium carboxymethylcellulose; ($C_8H_{15}NaO_8$) in nanoparticle form henceforth; Na-CMC NPs. The primary polymer has been extracted from the natural plant Eichhornia

Crassipes. TGA results reveal exitance of four decomposition stages. X-ray diffraction (XRD) revealing a semi-crystalline structure with a high degree of crystallinity (81 ± 1) % and nanoparticle sizes (11–40) nm. EDAX and SEM Scan confirm the formation of nano particle size of Na-CMC. It could be considered as a heavy metal absorber due to detected peaks found in FTIR and NMR. A detailed comparison with native cellulose has been discussed. Degradation kinetic parameters has been measured, using thermal analysis and four activation energies values have been calculated for four different stages. Owing to this high absorption capacity, Na-CMC NPs hydrogels show significant potential for various environmental, industrial, and medical applications.

The dielectric properties of CMC reveals that the relaxation activation energy is 0.13 ± 0.05 eV. The dielectric modulus analysis reveals that the material obeys Debye relaxation and X-ray studies reveals that the prepared CMC has Para-crystalline structure. The conduction mechanism is correlated barrier hopping mechanism (CBH). The decomposition temperatures effect on the dielectric constant and the conductivity of the prepared Na-CMC NPs polymer.

Acknowledgements The authors thanks Prof. Dr. Mohga F. Mostafa for experimental facilities in electromagnetic lab and helpful discussions. Prof. Dr. Hamada Mahmoud Dean of Faculty of Science Beni-Suef University for financial support needed to perform various analysis illustrated in the present work.

Author Contributions Samy A. Elsayed: Conceptualization, Supervision, Validation, Project administration, Writing- Original Draft, Data curation. M. A. Elhady: Editing Original Draft, Review & Editing, Visualization. A. K. Tammam: Software, Validation, Formal analysis, Data Curation, Resources, Review & Editing, Investigation, Formal analysis.

Funding Open access funding provided by The Science, Technology & Innovation Funding Authority (STDF) in cooperation with The Egyptian Knowledge Bank (EKB). This research received no financial support from any funding agency in the public or commercial.

Data Availability No datasets were generated or analysed during the current study.

Declarations

Conflict of interest The authors declare no competing interests.

Open Access This article is licensed under a Creative Commons Attribution 4.0 International License, which permits use, sharing, adaptation, distribution and reproduction in any medium or format, as long as you give appropriate credit to the original author(s) and the source, provide a link to the Creative Commons licence, and indicate if changes were made. The images or other third party material in this article are included in the article's Creative Commons licence, unless indicated otherwise in a credit line to the material. If material is not included in the article's Creative Commons licence and your intended use is not permitted by statutory regulation or exceeds the permitted use, you will need to obtain permission directly from the copyright holder. To view a copy of this licence, visit http://creativecommons.org/licenses/by/4.0/.

References

1. Tabata K et al (2024) Facile fabrication technique of polymeric ionic liquids-coated core-shell nanoparticles for polymer electrolyte membranes. Adv Sustain Syst 8(3):2300395
2. Ben Bakrim W et al (2022) *Eichhorniacrassipes* (Mart.) Solms: a comprehensive review of its chemical composition, traditional use, and value-added products. Front Pharmacol 13:842511
3. Zahran MA, Willis AJ (2008) The vegetation of Egypt, vol 2. Springer Science & Business Media
4. Djihouessi MB et al (2023) Paradigm shifts for sustainable management of water hyacinth in tropical ecosystems: a review and overview of current challenges. Environ Chall 11:100705
5. Jernelöv A (2017) The long-term fate of invasive species. Aliens forever or integrated immigrants with time, pp 1–296
6. He M et al (2025) Advances in polysaccharide-based antibacterial materials. Int J Biol Macromol 308:142598
7. Ayyadurai A, Saravanan MM, Devi M (2023) Integrated method for waste water treatment using water hyacinth and its application in concrete. Int J Adv Technol Eng Explor 10(109):1742
8. Venu H et al (2019) Eichhornia crassipes biodiesel as a renewable green fuel for diesel engine applications: performance, combustion, and emission characteristics. Environ Sci Pollut Res 26(18):18084–18097
9. Amalina F et al (2022) Water hyacinth (*Eichhornia crassipes*) for organic contaminants removal in water—a review. J Hazard Mater Adv 7:100092
10. Zubair M, Arshad M, Ullah A (2021) Nanocellulose: a sustainable and renewable material for water and wastewater treatment. Natural Polymers-based green adsorbents for water treatment. Elsevier, pp 93–109
11. Patel DK, Dutta SD, Lim KT (2019) Nanocellulose-based polymer hybrids and their emerging applications in biomedical engineering and water purification. RSC Adv 9:19143–19162
12. He M et al (2025) Research progress of the preparation of cellulose ethers and their applications: a short review. Molecules 30(7):1610
13. Florencio C et al (2024) Carboxymethylcellulose production from sugarcane bagasse: a new approach in biorefinery concept. Int J Biol Macromol 282:136998
14. Chen H et al (2019) Arsenic (iii) removal by nanostructured dialdehyde cellulose–cysteine microscale and nanoscale fibers. ACS Omega 4(26):22008–22020
15. Aly MI et al (2025) Adsorption behavior of cobalt-60 from aqueous solutions using polyacrylamide/gum acacia/cadmium oxide nano composite synthesized by gamma irradiation. Emergent Mater. https://doi.org/10.1007/s42247-025-01272-9
16. Tanpichai S et al (2022) Extraction of nanofibrillated cellulose from water hyacinth using a high speed homogenizer. J Nat Fibers 19(13):5676–5696
17. Liu Z et al (2024) Synthesis and characterization of novel water hyacinth (*Eichhornia crassipes*) biodegradable mulch films. Ind Crops Prod 222:119548
18. Elhady MA, Helal RH (2025) Gamma radiation synthesis of a humidity sensor hydrogel based on superabsorbent of poly sodium acrylate and poly N-isopropylacrylamide copolymer loaded with CaCl2 and charcoal. J Thermoplast Compos Mater 38:4141–4162
19. Pakutsah K, Aht-Ong D (2020) Facile isolation of cellulose nanofibers from water hyacinth using water-based mechanical

defibrillation: insights into morphological, physical, and rheological properties. Int J Biol Macromol 145:64–76
20. French AD (2014) Idealized powder diffraction patterns for cellulose polymorphs. Cellulose 21(2):885–896
21. Tribulová T et al (2019) The effects of transition metal sulfates on cellulose crystallinity during accelerated ageing of silver fir wood. Cellulose 26:2625–2638
22. Burakov AE et al (2018) Adsorption of heavy metals on conventional and nanostructured materials for wastewater treatment purposes: a review. Ecotoxicol Environ Saf 148:702–712
23. Okano T, Sarko A (1984) Mercerization of cellulose. I. X-ray diffraction evidence for intermediate structures. J Appl Polym Sci 29(12):4175–4182
24. Ward K Jr (1950) Crystallinity of cellulose and its significance for the fiber properties. Text Res J 20(6):363–372
25. Segal L et al (1959) An empirical method for estimating the degree of crystallinity of native cellulose using the X-ray diffractometer. Text Res J 29(10):786–794
26. He K et al (2018) Method for determining crystal grain size by X-ray diffraction. Cryst Res Technol 53(2):1700157
27. Williamson GK, Hall WH (1953) X-ray line broadening from filed aluminium and wolfram. Acta Metall 1(1):22–31
28. Zak AK et al (2011) X-ray analysis of ZnO nanoparticles by Williamson–Hall and size–strain plot methods. Solid State Sci 13(1):251–256
29. Ian J (1996) Langford and D. Louër. Rep Prog Phys 59:131–234
30. Biswal DR, Singh RP (2004) Characterisation of carboxymethyl cellulose and polyacrylamide graft copolymer. Carbohydr Polym 57(4):379–387
31. Joyline G et al (2023) High swelling carboxymethyl cellulose synthesized from coconut fibers. J Nat Fibers 20(2):2283549
32. Adinugraha MP, Marseno DW (2005) Synthesis and characterization of sodium carboxymethylcellulose from Cavendish banana pseudo stem (Musa cavendishii LAMBERT). Carbohydr Polym 62(2):164–169
33. Aly MI et al (2022) Eco-friendly polyvinyl alcohol/beeswax blend prepared using gamma irradiation for adsorption of cesium ions from an aqueous solution. Chem Ecol 38(10):949–966
34. Elhady MA, Mousaa IM, Attia RM (2022) Preparation of a novel superabsorbent hydrogel based on polyacrylic acid/shellac using gamma irradiation for adsorption removal of malachite green dye. Polym Polym Compos 30:09673911221074435
35. Tarabiah AE et al (2022) Enhanced structural, optical, electrical properties and antibacterial activity of PEO/CMC doped ZnO nanorods for energy storage and food packaging applications. J Polym Res 29(5):167
36. Rundle RE, Parasol M (1952) O–H stretching frequencies in very short and possibly symmetrical hydrogen bonds. J Chem Phys 20(9):1487–1488
37. Pimentel GC, Sederholm CH (1956) Correlation of infrared stretching frequencies and hydrogen bond distances in crystals. J Chem Phys 24(4):639–641
38. Saputra AH et al (2015) Synthesis and characterization of hydrogel from cellulose derivatives of water hyacinth (*Eichhornia crassipes*) through chemical cross-linking method by using citric acid. J Eng Sci Technol 10:75–86
39. Hemalatha K et al (2017) Effect of NiCuZnFe2O4 on the microcrystalline properties of PVA/CMC polymer blends. Mater Res Innovations 21(2):122–128
40. Bellamy LJ, Owen AJ (1969) A simple relationship between the infra-red stretching frequencies and the hydrogen bond distances in crystals. Spectrochim Acta A Mol Spectrosc 25(2):329–333
41. VanderHart DL, Atalla RH (1984) Studies of microstructure in native celluloses using solid-state carbon-13 NMR. Macromolecules 17(8):1465–1472
42. Kono H (2013) 1H and 13C chemical shift assignment of the monomers that comprise carboxymethyl cellulose. Carbohydr Polym 97(2):384–390
43. Spilker R (2016) Determination of anionic. Handbook Of Detergents, Part C: Analysis. p 215
44. Kittur FS et al (2002) Characterization of chitin, chitosan and their carboxymethyl derivatives by differential scanning calorimetry. Carbohyd Polym 49(2):185–193
45. Sharma M, Bajpai A (2018) Superabsorbent nanocomposite from sugarcane bagasse, chitin and clay: synthesis, characterization and swelling behaviour. Carbohydr Polym 193:281–288
46. Menczel JD, Prime RB (2009) Thermal analysis of polymers
47. Takigami M et al (2007) Preparation and properties of CMC gel. Trans Mater Res Soc Jpn 32(3):713–716
48. Coats AW, Redfern JP (1964) Kinetic parameters from thermogravimetric data. Nature 201(4914):68–69
49. McDonald RS (1957) Study of the interaction between hydroxyl groups of Aerosil Silica and adsorbed non-polar molecules by infrared spectrometry1. J Am Chem Soc 79(4):850–854
50. Yates DJC (1961) Infrared studies of the surface hydroxyl groups on titanium dioxide, and of the chemisorption of carbon monoxide and carbon dioxide. J Phys Chem 65(5):746–753
51. Wang J, Somasundaran P (2005) Adsorption and conformation of carboxymethyl cellulose at solid–liquid interfaces using spectroscopic, AFM and allied techniques. J Colloid Interface Sci 291(1):75–83
52. Shetty SK et al (2021) Dielectric relaxations and ion transport study of NaCMC: NaNO3 solid polymer electrolyte films. Ionics 27(6):2509–2525
53. Lotfy VF et al (2023) Toward pulping process for enhancing the RS-black liquors as precursor of activated carbons for aqueous adsorbent purposes. Sci Rep 13(1):20072
54. Hummel DO (1986) IR-Spektrometrie von Polymeren. In: Analytiker-Taschenbuch. pp 67–101
55. Atalla RH, Vanderhart DL (1984) Native cellulose: a composite of two distinct crystalline forms. Science 223(4633):283–285
56. Song W-Y, Zahra A, Shin S-J (2024) Interpretation of carboxymethylation in cellulose pretreatment by 1H-NMR spectroscopy. J Korea TAPPI 56(1):11–21
57. Fontana C, Widmalm G (2023) Primary structure of glycans by NMR spectroscopy. Chem Rev 123(3):1040–1102
58. Hosemann R, Hindeleh AM (1995) Structure of crystalline and paracrystalline condensed matter. J Macromol Sci B Phys 34(4):327–356
59. Bregado JL et al (2019) Amorphous paracrystalline structures from native crystalline cellulose: a molecular dynamics protocol. Fluid Phase Equilib 491:56–76
60. Basta AH (1998) Preparation, characterization and properties of paper sheets made from chemically modified wood pulp treated with metal salts. Int J Polym Mater 42(1–2):1–26
61. Friedman HL Kinetics of thermal degradation of char-forming plastics from thermogravimetry. Application to a phenolic plastic. Wiley Online Library
62. Vyazovkin S et al (2020) ICTAC Kinetics Committee recommendations for analysis of multi-step kinetics. Thermochim Acta 689:178597
63. El-Saied H et al (2008) Production and characterization of economical bacterial cellulose. BioResources 3(4):1196–1217
64. Priya G, Narendrakumar U, Manjubala I (2019) Thermal behavior of carboxymethyl cellulose in the presence of polycarboxylic acid crosslinkers. J Therm Anal Calorim 138:89–95
65. Nashar DEE, Abd-El-Messieh SL, Basta AH (2004) Newsprint paper waste as a fiber reinforcement in rubber composites. J Appl Polym Sci 91(5):3410–3420

66. Tammam AK, Kahlifa Z, Elsayed SA (2020) First and second phase transition discovery in amorphous chalcogenide Se60Te30S10 composition. J Non-Cryst Solids 529:119729
67. Abdeldaym A, Elhady MA (2019) Investigation of the effect of aluminum oxide nanoparticle additives and gamma irradiation on the thermal behavior of syndiotactic polystyrene. Polym Compos 40(9):3588–3600
68. Shetty SK et al (2021) Dielectric relaxations and ion transport study of NaCMC: NaNO 3 solid polymer electrolyte films. Ionics 27:2509–2525
69. Nelson SO, Bartley PG (2002) Frequency and temperature dependence of the dielectric properties of food materials. Trans ASAE 45(4):1223
70. de Britto D, Assis OBG (2009) Thermal degradation of carboxymethylcellulose in different salty forms. Thermochim Acta 494(1–2):115–122
71. Sharaf A et al (2023) Synthesis and characterization of gamma irradiated polyvinyl chloride/graphite carbon nitride nanocomposite films for electronic applications. J Thermoplast Compos Mater 36(12):4841–4857
72. Feldman Y, Gusev YA, Vasilyeva MA (2012) Dielectric relaxation phenomena in complex systems. Tutorial, Kazan Federal University, Institute of Physics
73. Semmar N, Tanguier JL, Rigo MO (2003) Specific heat of carboxymethyl cellulose and Carbopol aqueous solutions. Thermochim Acta 402(1–2):225–235
74. Nessim RI et al (1993) Frequency dependence of the complex dielectric constant of sodium carboxymethyl cellulose. Angew Makromol Chem 204(1):51–61
75. Mostafa MF, Youssef AAA (2004) Magnetic and electric studies of a new Cu (II) perovskite-like material. Z Naturforsch A 59(1–2):35–46
76. Abdeldaym A, Elhady MA (2020) Role of copper oxide nanoparticles and gamma irradiation in optimising mechanical and the DC-electrical properties of nylon 66. J Compos Mater 54(24):3595–3610
77. Macedo PB, Ct M, Bose R (1972) The role of ionic diffusion in polarisation in vitreous ionic conductors
78. Turky G et al (2021) Carboxymethyl cellulose-based hydrogel: dielectric study, antimicrobial activity and biocompatibility. Arab J Sci Eng 46(1):17–30
79. Mousaa IM et al (2023) Development of a highly hydrophobic and antimicrobial surface for polyester fabrics treated with (vinyl acetate versatic ester/paraffin wax) blend containing sodium chloride using electron beam irradiation. Prog Org Coat 174:107230
80. El-Sayed NS et al (2019) Development of electrical conducting nanocomposite based on carboxymethyl cellulose hydrogel/silver nanoparticles@ polypyrrole. Synth Met 250:104–114
81. Mostafa MF, El-Khiyami SS, Tammam AK (2022) Dielectric, conductivity relaxation, conduction mechanisms and thermal behavior in 2-D Ruddlesden-Popper manganese bromide perovskite hybrid. Mater Chem Phys 290:126526
82. Mostafa MF, Tammam AK (2024) Crystal structure, phase transitions, dielectric and conduction mechanisms of the new long chain organic-inorganic hybrid [(CH2) 8 (NH3) 2] CoCl4. Phys Scr 99(2):025948
83. Gargallo L, Radic D (2009) Physicochemical behavior and supramolecular organization of polymers. Springer Science & Business Media
84. Lataoui R et al (2023) Conduction mechanisms and complex impedance analysis in La0. 6Sr0. 4FeO3 ceramic. J Electroceram 50(4):121–138
85. El-Nahass MM, Zayed HA, Ali HAM (2021) Characterization of structural, electrical conductivity and dielectric properties of 1', 3'-dihydro-1', 3', 3'-trimethyl-6-nitrospiro [2H-1benzopyran-2, 2'[2H] indole] compound. J Sci Res Sci 38(part 1 (Basic Sciences)):36–57
86. Elhady MA et al (2024) Fabrication and application of novel magnetic polyethylene oxide/polyacrylamide/graphitic carbon nitride nanocomposite by gamma irradiation for metal ion removal from waste water. Int J Environ Anal Chem 104(20):9035–9060

Publisher's Note Springer Nature remains neutral with regard to jurisdictional claims in published maps and institutional affiliations.